Title:

Pneumococcus uses COMMD2 to alter host cellular immunity.

Authors: Michael G. Connor[1*], Lisa Sanchez[2], Christine Chevalier[1], Tiphaine M. N. Camarasa[1], Filipe Carvalho[3], Matthew J.G. Eldridge[1], Thibault Chaze[4], Mariette Matondo[4], Esma Karkeni[5], Sara Dufour[6], Francis Impens[6], Sebastian Baumgarten[7], Jost Enninga[2], Melanie A. Hamon[1*].

Affiliations:

1 Chromatin and Infection, Institut Pasteur, Paris, France.

2 Dynamics of Host–Pathogen Interactions Unit, Institut Pasteur, & UMR CNRS, Paris, France.

3 Institut MICALIS (UMR 1319) INRAE, AgroParisTech, Université Paris-Saclay

4 Institut Pasteur, Université de Paris Cité, CNRS UAR2024, Proteomics Platform, Mass Spectrometry for Biology Unit, 75015 Paris, France.

5 Single Cell Biomarkers UTechS, Institut Pasteur, Université Paris Cité, Paris, France.

6 VIB-UGent Center for Medical Biotechnology, VIB Proteomics Core, VIB, Department for Biomolecular Medicine, Ghent University, Ghent, Belgium.

7 Institut Pasteur, Université Paris Cité, Parasite RNA Biology, F-75015 Paris, France

*Correspondence:

Michael G. Connor (mconnor@pasteur.fr) & Melanie A. Hamon (melanie.hamon@pasteur.fr)

Abstract:

NF-κB driven cellular immunity is essential for both pro- and anti-inflammatory responses to microbes, which makes it one of the most frequently targeted pathways by bacteria during pathogenesis. How NF-κB tunes the epithelial response to *Streptococcus pneumoniae* across the spectrum of commensal to pathogenic outcomes is not fully understood. In this study, we compare a commensal-like 6B ST90 strain to an invasive TIGR4 isolate and demonstrate, through comparative mass spectrometry of the p65 interactome, TIGR4 challenge triggers a novel interaction of COMMD2 with p65 and p62. Mechanistically, we show this complex mediates export of p65 for degradation and COMMD2 is necessary for altering host cellular immunity. With these results, we reveal for the first time a new bacterial pathogenesis mechanism to repress host inflammatory response though COMMD2 and p65 degradation while presenting a paradigm for diverging NF-κB responses to pneumococcus.

Introduction:

Airway epithelial cells, which line the entirety of the human respiratory tract, play a key role in both driving and shaping the host inflammatory and homeostatic response(s) to both pathogenic and commensal microbes [1-3]. Indeed, defining molecular processes of bacterial-host crosstalk at this interface has emerged as a key determinant shaping how bacterial pathobionts escape from asymptomatic carriage within the human upper respiratory tract (URT) to become pathological agents causing symptomatic disease. In fact, for human restricted pathobionts, such as *Streptococcus pneumoniae* (the pneumococcus), *Haemophilus influenzae*, *Moraxella catarrhalis*, and *Staphylococcus aureus,* colonization of the human URT is critical for maintenance of their natural reservoir and a prerequisite for potentially lethal disease [4,5]. Yet mechanistic understanding of the cellular processes involved in compartmentalizing commensal-like versus pathogenic host outcomes to these pathobionts remains unclear.

We previously showed that isolates of *Streptococcus pneumoniae* drive differential host responses by fine tuning airway epithelia cellular immunity [6-12]. A commensal-like serotype 6B ST90 CC156 lineage F isolate, in contrast to an invasive favoring TIGR4 isolate, triggered a unique NF-κB signature through the chromatin remodeler KDM6B, that was required for host mediated confinement to the upper respiratory tract in a murine infection model. Surprisingly, these studies also revealed that the pathogenic *S. pneumoniae* strain TIGR4 largely suppressed NF-κB activation and downstream gene transcription [6]. As the eukaryotic NF-κB family of transcriptional regulators are well documented for their potent ability to drive both pro- and anti-inflammatory cellular immune responses during microbe-host interaction, we sought to better define this dichotomy [13-15].

To date, a large majority of bacterial virulence phenotypes either co-opt NF-κB repressors or directly target NF-κB pathway components using virulence factors (general review [15,16]). Generally, upon sensing of inflammatory molecules, such as cytokines (IL-1β or TNFα), pathogen-associated molecular patterns (PAMPs; i.e. lipopolysaccharide), or danger-associated molecular patterns (DAMPs; i.e. IL-1α or nuclear protein HMGB1), NF-κB subunits are rapidly activated by phosphorylation on serine residues (S536 and S276). Simultaneously, NF-κB dimers are released from their inhibitory IkB proteins and translocated to the nucleus for additional modification. Ultimately, this process leads to the binding of activated dimers to cognate NF-κB DNA motifs, thereby inducing NF-κB dependent gene transcription. NF-κB activation is tightly controlled for precise and rapid induction, but also for prompt repression. NF-κB dimers can be repressed through extraction, sequestration, and degradation from within the nucleus, while in parallel blocking cytoplasmic activation and promoting transcription of negative regulators [17,18,20,22-26]. However, in contrast to the myriad of studies on activators only a few negative regulators of NF-κB and their pathways have been documented.

COMMD (copper metabolism gene MURR1 domain)[27] proteins are among the select few known negative regulators of NF-κB [25,27-32]. There are ten members of the COMMD family, all of which, interact with NF-κB to regulate signaling. The best-studied architype member, COMMD1, upon stimulation by TNF will lead to extraction of p65 from chromatin, followed by ubiquitination and

proteasomal degradation. This process functions independently of NF-κB nuclear translocation and IkBa, but through association with Cullin proteins, is able to terminate NF-κB signaling [25,27,29-35]. For the other COMMD proteins, however, neither their functional activity, their mechanism of NF-κB repression, or their interacting partners, outside of cullins, are known.

Here, we demonstrate that a pathogenic TIGR4 pneumococcal strain [6], in contrast to a commensal-like 6B ST90 isolate [6], represses phosphorylation and activation of NF-κB p65. In fact, TIGR4 infection leads to specific degradation of p65 in airway epithelial cells, even upon stimulation with a strong inflammatory agonist, IL-1β. We performed an interactome of p65 and show that each pneumococcal strain interacts with diverging p65 interacting partners, revealing an original aggrephagy mechanism involving COMMD2 and p62. Furthermore, our studies on the understudied functionality of COMMD2 by RNAi demonstrated it is necessary in regulating host cellular immunity both basally and during pneumococcal challenge. Finally, deeper investigation of the COMMD2 interactome in comparison to the 6B ST90 isolate and under stimulation with the potent pro-inflammatory cytokine IL-1β revealed further specificity during TIGR4 challenge, with its COMMD2 interactome enriching for additional transcriptional and translational components. Altogether, we report a novel mechanism of pathogenesis to degrade p65 and repress the host response that is specifically induced by TIGR4.

Results:

TIGR4 engages a divergent NF-κB p65 interactome in comparison to commensal-like 6B ST90.

We previously showed that TIGR4, in comparison to 6B ST90 (hereafter 6B), induced a transcriptionally different NF-kB dependent response, which was largely associated with gene repression [6]. To understand NF-κB p65 activation differences between the invasive TIGR4 and commensal-like 6B pneumococcal isolates we performed mass spectrometry of NF-κB p65 (Fig. 1A). An A549 GFP-p65 cell line was challenged with either TIGR4 or 6B and 2 hrs post-challenge GFP-p65 was immunoprecipitated with a matched A549 GFP alone control for mass spectrometry interactome analysis along with p65 posttranslational modifications (Fig. 1B; Sup. Table 1).

Analysis of the individual TIGR4 and 6B volcano plots in comparison to GFP alone showed specific enrichment for known NF-kB p65 associated partners (blue), reflecting the robustness of our A549 GFP-p65 cell line (Fig. 1C & D). GO ontology analysis of these individual p65 interactomes to GFP alone showed TIGR4 enriched for cellular trafficking components along with p62/SQSTM1 (Fig. 1C; Sup. Fig 1A), whereas the interactome of 6B reflected enrichment for classical NF-kB signaling components and signaling processes (Fig. 1D; Sup. Fig 1B). While the overall interactomes of TIGR4 and 6B appear similar, deeper investigation revealed key differences. This agrees with our previous findings demonstrating fine-tuning of NF-kB p65 signatures between TIGR4 and 6B was essential for commensal-like vs. invasive host responses [6].

However, to directly investigate any divergent p65 interactors between the TIGR4 and 6B datasets we compared the interactomes against each other (Fig. 1E). This comparison showed lower overall association of known NF-κB partners for TIGR4 alongside significant specific enrichment for COMMD proteins (2 & 4) and proteins associated with degradation/ubiquitin pathways (HDAC6, UBE2C…) by GO ontology (Fig. 1E & F; Sup. Table 1) [36].

Indeed, p62 and HDAC6 are classical mediators of aggrephagy, which is a form of selective autophagy to degrade protein aggregates [36-38]. Interestingly, it has also been shown that abnormal NF-kB p65 activation may be a signal p62 mediated turnover [39]. Moreover, COMMD proteins, such as COMMD2, are known to negatively regulate NF-kB family members through degradation [27,29,30,34,35,40]. Of the two COMMD proteins found in our TIGR4 dataset, COMMD2 was previously shown, by ectopic expression, to reside in the cell cytosol and had a higher association with RelA and NF-κB1 [27,35]. Therefore, our proteomic data suggested that p65 could be targeted for degradation through an aggrephagy pathway under TIGR4 infection conditions.

TIGR4 differentially engages NF-κB p65 in comparison to commensal-like 6B ST90.

125 Previously, we clearly showed commensal-like 6B pneumococcal strain activates p65 to drive a unique
126 inflammatory signature in comparison to a disease causing TIGR4 strain [6,41]. Interestingly, this was also
127 seen in kinetic NF-kB dependent gene expression profiles when comparing TIGR4 to 6B and a positive
128 control IL-1β [6,41]. Given our previous findings and the mass spectrometry data showing enrichment for
129 aggrephagy, we hypothesize that TIGR4 disrupted NF-κB activation. To directly test the NF-κB
130 activation hypothesis, we challenged A549 cells with either TIGR4 or 6B ST90 alone, or in combination
131 with IL-1β, a pro-inflammatory stimulus known to induce p65 phosphorylation of key serine residues
132 536 and 276 (review [23]). Cells were collected 2hr post-challenge for immunoblotting to determine the
133 total levels of p65 and phosphorylated p65. The ratio of phos-S536 to total p65 between TIGR4 and
134 6B (± IL-1β) against the IL-1β control showed decreased levels, whereas the ratio of phos-S276 to total
135 p65 showed minimal differences (Fig. 2A – C). Curiously, for all TIGR4 challenge groups total level of
136 p65 was significantly reduced (pV ≤ 0.01) compared to uninfected, IL-1β or 6B exposed cells (Fig. 2B).
137 Thus, we compared phosphorylated p65 S536 and S276 to actin in order to determine whether TIGR4
138 challenge reduced their total cellular pool. Indeed, from this analysis it was clear that TIGR4 in
139 comparison to 6B, reduced the total cellular amount of S536 p65 and not S276 (Sup. Fig. 2 A & B).
140 Moreover, through cross-comparison between TIGR4 and 6B (± IL-1β) a trend emerged that either
141 TIGR4 condition reduced total p65 S536 or S276 amounts, with the most substantial difference being
142 on levels of p65 S536 (Sup. Fig. 2 A & B). Next, we tested whether TIGR4 challenge also lowered the
143 level of p65 S536 phosphorylation in primary human nasal epithelial cells, since *S. pneumoniae* is an
144 opportunistic respiratory pathogen that primarily colonizes first the upper airway epithelial cells. Our
145 results showed a comparable trend for TIGR4 (± IL-1β) in comparison to uninfected, IL-1β or 6B.
146 Importantly in TIGR4 lysates the total levels of p65, S536 and S276 were decreased in comparison to
147 uninfected, IL-1β and 6B groups (Sup. Fig. 2C). Altogether, these data clearly indicated that TIGR4
148 challenge reduced total amounts of p65, phos-S536 and phos-S276, which primarily affected the ratio
149 of phos-S536 to total p65, and aligned well with the interactome data.
150 As p65 phos-S536 is a marker reflecting p65 nuclear translocation (review [23]), our observations
151 that TIGR4 challenge resulted in significant difference in the S536 / p65 ratio raised the possibility that
152 TIGR4 challenge induced differential nuclear localization kinetics in comparison to 6B. To assess this
153 we completed time course microscopy of A549 cells to evaluate nuclear S536 levels by
154 immunofluorescence, as this reflects p65 translocation post liberation from the cytoplasmic NEMO
155 complex (review [23]). For this, we segmented on cellular nuclei (Draq5) and quantified nuclear p65 S536
156 intensity (Fig. 2E & F). Our kinetics show nuclear S536 profile between TIGR4 and 6B differs. TIGR4
157 leads to a slow and modest increase starting at 10 minutes and peaks at 90 mins before coming back
158 down. In contrast 6B kinetics mirror the positive control, IL-1β, with a rapid increase by 10 minutes
159 followed by a gradual decline (Fig. 2E & F). When A549 are challenged with either TIGR4 or 6B in
160 combination with IL-1β, the levels of nuclear S536 increase rapidly for both, similarly to IL-1β alone.
161 These data supported differences observed by immunoblot, whilst suggesting that TIGR4 (± IL-1β) was
162 triggering aberrant and low level p65 activation in comparison to IL-1β and 6B.
163 Since we previously showed that TIGR4 alone, in comparison to 6B and IL-1β, drove minimal
164 NF-kB p65 dependent gene expression kinetically [6,41], we tested if IL-1β at the time of challenge could
165 restore expression profiles to TIGR4. Total RNA was periodically collected from A549 cells out to 120
166 minutes post challenge with TIGR4 (± IL-1β) and IL-1β alone. Relative expression was determined for
167 CFS2 and PTGS2 (COX-2) against uninfected/untreated controls at each time point. TIGR4 in
168 comparison with IL-1β alone did not lead to activation of any of the genes out to 2h post challenge,
169 which aligns with our previous findings [6] (Sup. Fig. 2D & E). Furthermore, under conditions where IL-
170 1β was added during TIGR4 challenge, there was both a delay and a repression of these transcripts in
171 comparison to IL-1β alone.
172 Transcriptional activation by p65 requires its binding to cognate kappa-binding sites at the
173 chromatin level. Therefore, we evaluated levels of chromatin bound p65 at the locus of the NF-κB
174 dependent gene *PTGS2* and *CSF2* as these two genes had striking transcriptional profiles. Chromatin
175 was collected from A549 cells 2 hrs post-challenge with TIGR4 (± IL-1β) and the recovery of p65

176 quantified against uninfected and IL-1β controls by ChIP-qPCR targeting kappa-binding sites upstream
177 of the *PTGS2* and *CSF2* transcriptional start site (Sup. Fig. 2F - H). For both genes TIGR4 challenged
178 cells resulted in less than 5% recovery of p65. This stands in contrast to the three-fold higher p65
179 recovery in IL-1β alone (Sup. Fig. 2G & H). Interestingly, in the TIGR4 + IL-1β condition p65 recovery
180 was comparable to IL-1β alone (Sup. Fig. 2G & H). Therefore, the lack of p65 driven transcription under
181 TIGR4 challenge is intrinsically due to the absence of p65 at the chromatin. Altogether, these results,
182 in combination with our previous findings, show that TIGR4, in contrast to the IL-1β, is driving
183 dysfunctional p65 signaling [6,41].
184
185 Blocking autophagy increases cytoplasmic COMMD2, p62 and p65 levels.
186 To study the localization of COMMD2, we generated a COMMD2 cell line. Strikingly, upon
187 TIGR4 challenge of the GFP-COMMD2, we observed by microscopy that TIGR4 drove COMMD2
188 localization to the nucleus. COMMD2 is an otherwise cytoplasmic protein containing two nuclear
189 export signals [34,35,43]. We confirmed this translocation by immunoblotting GFP-COMMD2 cell
190 fractionations obtained from cells challenged with TIGR4 (± IL-1β) alongside from uninfected and IL-
191 1β controls (Sup. Fig. 3A – C). Cells treated with IL-1β or uninfected had 20% COMMD2 in the nucleus,
192 in contrast to that of TIGR4 (± IL-1β) which showed 80% of COMMD2 was nuclear (Sup. Fig. 3B). Finally,
193 we tested if the commensal-like strain 6B ST90 could also induce COMMD2 nuclear localization.
194 Immunoblotting of cell fractions of the GFP-COMMD2 we show 6B ST90 was incapable of triggering
195 nuclear localization of COMMD2 (Sup. Fig. 3C). Thus, these data demonstrate TIGR4 specifically
196 triggers COMMD2 nuclear localization.
197 Using the COMMD2 cell line, we tested the effect of blocking aggrephagy with Bafilomycin A1
198 on the levels of p65, p62 and COMMD2, 2 hrs post-challenge with either IL-1β or TIGR4 (± IL-1β; MOI
199 20) using confocal microscopy (Fig. 3A – F; rep. images Sup. Fig. 4 p65 & Sup. Fig. 5 p62). Baf. A1
200 treatment had minimal effect on total or nuclear COMMD2 for uninfected and IL-1β, whereas TIGR4
201 (± IL-1β) stimulation significantly (pV ≤ 0.001) increased total COMMD2 (Fig. 3 A &B). Interestingly,
202 there was a slight inverse decrease in TIGR4 (± IL-1β) nuclear COMMD2 – strongly supporting a role
203 for aggrephagy in cytoplasmic turnover. Similarly to COMMD2, TIGR4 (± IL-1β) challenged cells treated
204 with Baf. A1 displayed an increase in p62, and restored p65 levels comparable to uninfected controls
205 (Fig. 3C - F). Moreover, in Baf. A1 treated cells challenged with TIGR4 the area of p65 and p62 puncta
206 increased, which is a conventional phenotype associated with blocked autophagosomes (Fig. 3G & H;
207 rep. images Sup. Fig. 4 p65 & Sup. Fig. 5 p62).
208 Overall, the combination of these data clearly shows TIGR4 challenge of airway epithelial cells
209 specifically led to COMMD2 nuclear localization and aggrephagy, a largely cytoplasmic process,
210 contributing to reduce the levels of p65 and COMMD2 within the cell.
211
212 COMMD2 is associated with both p65 and p62.
213 To further test the aggrephagy hypothesis, we wanted to determine whether COMMD2, p65
214 and p62 formed a complex; thus, a plausible explanation why blocking aggrephagy with Baf. A1 would
215 increase all three of these components. Currently, the only commercial COMMD2 antibody has limited
216 suitability for immunoprecipitation or immunofluorescence, thus, we used the GFP-COMMD2 cell line.
217 For this we challenged cells with either 6B ST90 (± IL-1β), TIGR4 (± IL-1β) or IL-1β controls for 2h and
218 performed immunoprecipitation of GFP-COMMD2 from cell lysates. Samples were probed for p65 or
219 p62 to detect interaction with COMMD2. Our results show that only under TIGR4 challenge conditions
220 do p65 and p62 interact with COMMD2 (Fig. 4A & B). Furthermore, upon addition of IL-1β, p65
221 interacts with COMMD2 to even higher levels.
222 To evaluate complex formation in primary cells, we collected lysates from primary nasal cells
223 challenged with either TIGR4 or 6B, as well as from uninfected controls. We performed p65
224 immunoprecipitation and tested whether TIGR4 could drive an endogenous native interaction of p65
225 with COMMD2 (Sup. Fig. 6A). Samples were probed for p65 and COMMD2 prior to being revealed with
226 the VeriBlot secondary HRP antibody. This secondary HRP antibody does not recognize denatured

227 heavy and light chain IgG, which would otherwise occur closely to our targets potentially masking
228 positive bands (65kda & 25kda). Our results showed a 4-fold increase in COMMD2 interaction with
229 p65 under TIGR4 challenge (Sup. Fig. 6B). However, there was a significant reduction of the detected
230 levels of COMMD2 and p65 under TIGR4 conditions in comparison to uninfected or 6B (Sup. Fig. 6C
231 &D). This is consistent with results shown above and degradation of COMMD2 and p65 by aggrephagy.
232 Interestingly, there was a weight shift of COMMD2 in the p65 IP, suggestive of posttranslational
233 modification – known to occur on COMMD proteins. Therefore, COMMD2 is a new TIGR4 induced
234 interacting partner of p65 and is a component of a p65-COMMD2-p62 complex.
235
236 <u>COMMD2 exports p65 for lysosomal degradation.</u>
237 It is known that the architype COMMD family member, COMMD1, undergoes
238 nucleocytoplasmic trafficking [25,35,42]. Given that aggrephagy primarily occurs in the cellular cytosol, we
239 reasoned that aberrantly phosphorylated p65 during TIGR4 challenge led to nuclear translocation of
240 COMMD2, which in turn was involved with facilitating nuclear export of these p65 complexes.
241 Therefore, we tested whether COMMD2 was exported through CRM1 by using the
242 Leptomycin B inhibitor [43]. GFP-COMMD2 cells were treated with Leptomycin B (10 nM) prior to
243 immunofluorescence imagining of p62 and p65. Strikingly, blocking nuclear export resulted in
244 COMMD2, p62 and p65 now becoming localized to the nucleus even in uninfected and IL-1β treated
245 cells. In fact, COMMD2 and p62 were detected within nuclear puncta (Fig. 5A) where p65 was located
246 (Fig. 5B). Notably, our IL-1β positive pro-inflammatory stimulus control, known to drive nuclear
247 translocation of p65, had a significant (pV ≤ 0.0001) increase in the nuclear level of COMMD2 and p62
248 in comparison to treated cells (Fig. 5C & D). These surprising data suggest that under nuclear export
249 blockage, which occurs with Leptomycin B treatment [43], COMMD2 and p62 are naturally recruited to
250 the nucleus at specific puncta through a defined process.
251 Interestingly, upon challenge with TIGR4, Leptomycin B treated cells displayed higher levels
252 of COMMD2 and p62 accumulation in the nucleus than without treatment (Fig. 5A, C & D). Thus, upon
253 inhibiting nuclear export of COMMD2 and p62, these proteins are no longer degraded upon infection
254 and accumulate in the nucleus. Although COMMD2 and p62 puncta are observed upon addition of
255 Leptomycin B, the substantial amount of p65 trapped within the nucleus of these cells rendered
256 definitive scoring of puncta and colocalization for both difficult. Due to this, we measured a tangent
257 line (20 µm) across observed local maxima intensity "spots" to overlay the traces of p62 and p65 with
258 COMMD2 in uninfected, IL-1β and TIGR4 conditions demonstrating that indeed p62 and p65
259 associated with COMMD2 (Fig. 5C & D). Quantification of the total nuclear COMMD2 intensity
260 however showed inhibition of CRM1 did not increase total levels in comparison to untreated across
261 all groups (Fig. 5E). Thus, Leptomycin B inhibition led to concentrated accumulation of COMMD2 into
262 puncta. In contrast, Leptomycin B inhibition increased both p62 and p65 nuclear levels in all conditions
263 compared to untreated cells (Fig. 5F & G). Furthermore, under conditions of TIGR4 + IL-1β and
264 Leptomycin B inhibition, we observed a significant (pV ≤ 0.0001) increase in p62 puncta compared to
265 TIGR4 alone (Sup. Fig. 7A & B). These data show that TIGR4 challenge leads to an active CRM1
266 dependent export of p65 and the COMMD2 complex.
267
268 <u>The TIGR4 COMMD2 interactome is unique and enriched for NF-kB associated partners.</u>
269 Our results to this point clearly show the role of COMMD2–p65 during TIGR4 bacterial
270 challenge is unique even with respect to IL-1β. However, to date knowledge of COMMD protein
271 interacting partners and biological roles are largely centered around their interactions with NF-κB
272 subunits and cellular processes of trafficking, proteasome degradation and transcription [25,31,44,45], with
273 limited understanding of their potential mechanisms or impact during bacterial infection.
274 To deepen our investigation of TIGR4 induced COMMD2-p65 interaction and better define a
275 biological role for it during bacterial challenge, we assessed the COMMD2 interactome by mass
276 spectrometry (Fig. 6A-D). For this we immunoprecipitated GFP-COMMD2 from A549 cells 2 hrs post-
277 challenge with either TIGR4, 6B ST90 or our positive inflammatory control IL-1β for comparison against

278 uninfected. Pointedly in this mass spectrometry study we used the cross-comparison of GFP-COMMD2
279 against GFP alone to control for both non-specific COMMD2 complexes and artifacts which may be
280 intrinsic to ectopic expression (Sup. Fig. 8A; Sup. Table 2). The results of this comparison identified
281 known COMMD2 associations with other COMMD proteins, Commander and Retriever complexes
282 (CCDC22, CDC93, VPS35L, COMMD6, COMMD2, COMMD1, COMMD4, COMMD8, COMMD9,
283 COMMD3 & VPS29) [46], which further strengthens the robustness of our approach.
284 In contrast to 6B and IL-1β volcano plots, TIGR4 prompted positive enrichment for p65 (RelA),
285 p62 (SQSTM1) and HDAC6, which is another aggrephagy associated protein (Fig. 6B-C). Notably, for IL-
286 1β, the volcano plot shows none of the significant partners of COMMD2 held any known NF-kB
287 association (via BioGRID) at 2hrs (Fig. 6D). Moreover, there was a 5- and 80-fold higher recovery of
288 significantly enriched interacting partners under the TIGR4 condition compared to 6B ST90 and IL-1β
289 respectively (Fig. 6B-D; Sup. Table 3). Cross comparing these targets, we discovered that 254 unique
290 proteins were associated with COMMD2 under TIGR4 challenge with 92 of them being also found in
291 our p65 interactome dataset (Fig. 6E; Sup. Table 1). Remarkably overall this unique comparison of the
292 COMMD2 interactome datasets clearly supported the specificity of COMMD2 – p65 (RelA) during
293 TIGR4 challenge.
294 Finally, analysis using Panther ontology protein class of the significant targets obtained from
295 the interactome underscored a unique TIGR4 enrichment for host metabolite and protein modifying
296 enzymes as well as proteins associated with translation (Fig. 6F). From the analysis we also identified
297 a putative COMMD2 posttranslational modification associated with ubiquitination at Lysine residue
298 50 (Sup. Table 2), which aligns with our previous endogenous co-immunoprecipitation of COMMD2-
299 p65 (Sup. Fig. 6A). Altogether, these results showed during TIGR4 challenge COMMD2 function was
300 specific with a potential role in host inflammatory response.
301
302 <u>COMMD2 is a selective negative regulator of host cellular immunity.</u>
303 Having previously shown TIGR4 directly represses host transcription and in particularly NF-kB
304 dependent targets [6,41], we speculated that COMMD2 was required to alter NF-κB p65 driven host
305 immunity upon stimulation with TIGR4. Thus, inhibiting COMMD2 would lead to increased cytokine
306 production. To our knowledge, no direct chemical inhibitors of COMMD2 exist, so we used RNAi to
307 knockdown COMMD2 and p62 in primary human nasal epithelial cells (Sup. Fig. 9A-C). Whereas both
308 siRNAs to COMMD2 or their mixture resulted in 50-60% reduction, a single siRNA to p62 reduced the
309 target >70% (Sup. Fig. 9C). While knockdown of COMMD2 was not ideal it was consistently greater
310 with the second siRNA, thus we proceeded with bacterial challenge suspecting this minimal reduction
311 in COMMD2, in comparison to scrambled or p62, would be enough to discern roles for COMMD2
312 and/or p62 upon the analytes within our Luminex panel.
313 Following 48hrs of either Scrambled (Scr), COMMD2 or p62 RNAi primary human nasal cells
314 were challenged for 4 hrs with either IL-1β, TIGR4 or 6B (± IL-1β), with post-challenge supernatants
315 collected for Luminex (27-plex; COMMD2 Fig. 7A; Scr Sup. Fig. 9D; p62 Sup. Fig. 9E). Strikingly
316 COMMD2 RNAi resulted in selective elevation of multiple targets, even in the uninfected group, with
317 several being significantly higher than their respected scr control (pV reported; Fig. 7A). These analytes
318 - CCL20, CXCL1, CXCL10, IL-1ra, IL-8 and PTX3 - either border or were significantly different with
319 respect to each sample scr control. Interestingly, CCL20, CXCL1, CXCL10, IL-1ra, and IL-8 were also
320 elevated in the p62 RNAi data (Sup. Fig. 9E). Given this surprising result, we determined whether
321 COMMD2 RNAi impacted uninfected, IL-1β, TIGR4 or 6B equally. For this we first compared the
322 absolute difference of COMMD2 RNAi to scr (Fig. 7B). Our results showed that while on average TIGR4
323 challenge of COMMD2 RNAi cells increased all 27 analytes in comparison to 6B and uninfected cells
324 these elevated levels remained comparable to the IL-1β treated control. However, to assess the
325 degree in which COMMD2 or p62 RNAi affected TIGR4 or 6B we compared each RNAi condition to the
326 scr control (Fig. 7B). This comparison clearly showed knockdown of COMMD2 and p62 during TIGR4
327 challenge had far more impact on the profiles of the 27 analyte examined than for 6B. Altogether,
328 these data show that: 1) COMMD2, and likely p62, have a role in regulating specific cellular immunity

329 molecules in uninfected cells, and 2) TIGR4 relies on both COMMD2 and p62 to alter secreted host
330 immunity analytes.
331 Due to this, we explored whether a commonality existed in predicted NF-kB p65 (RelA) binding
332 motifs among these targets transcriptional start site (TSS). Herein, we pulled ± 2kb surrounding the
333 gene TSS (UCSC genome browser) for Transcription factor Affinity Prediction (TRAP) analysis [47] and for
334 comparison of the NF-kB motif to the canonical motif (JASPAR). Mapping predicted NF-kB motifs from
335 the COMMD2 targets did reveal several. However, there was no apparent commonality in location or
336 binding affinity of these predicted motif sites in this small dataset (Fig. 7C). However, the NF-kB motif
337 consensus sequence of the small COMMD2 targets, in comparison to the canonical motif using
338 Weblogo [48], showed a subtle change with higher probability of G/A (pos. 3) and C/T (pos. 7; Fig. 7D).
339 Interestingly, p62 RNAi also resulted in selective elevation of CCL20, CXCL1, CXCL10, IL-1ra, IL-8, SPI,
340 CXCL2, IL-6, MMP-1 and TNFα in one or more samples (Sup. Fig. 9E). CXCL10, even in uninfected
341 samples, was significantly increased (p value reported) under both COMMD2 and p62 RNAi conditions,
342 potentially suggesting a role of each in its regulation.
343 Overall, these results are the first evidence that COMMD2 is indeed a selective negative
344 regulator of NF-kB dependent gene transcription. Moreover, analysis of the targeted genes suggests
345 an unknown chromatin level component in the role of COMMD2 – p65 for gene expression.
346
347 <u>COMMD2 nuclear translocation favors invasive pneumococcal strains.</u>
348 Since COMMD2 nuclear localization only occurred during TIGR4 challenge we sought to
349 substantiate whether key TIGR4 virulence determinants were responsible. We first investigated
350 whether Pneumolysin (Ply) or hydrogen peroxide production via Pyruvate oxidase (SpxB) were
351 responsible for COMMD2 nuclear translocation.
352 Herein, we challenged GFP-COMMD2 cells with the ΔPly or ΔSpxB TIGR4 mutants alongside
353 their parental wildtype strain (Fig. 8A). Comparing ΔSpxB to ΔPly and their parental wildtype showed
354 that a ΔPly mutant does not trigger translocation, whereas the ΔSpxB mutant induced a partial
355 phenotype with ΔSpxB increasing nuclear COMMD2 levels over ΔPly but remaining at 75-80% of
356 wildtype (Fig. 8B). Given this result, we tested if a functional pneumolysin pore was required. For this
357 we used the JWTIGR4 ΔPly W433F pore mutant [49,50]. This mutant did not induce COMMD2
358 translocation (Fig. 8B). Altogether we concluded that COMMD2 translocation was dependent on
359 Pneumolysin pore formation in combination with SpxB.
360 However, the ΔSpxB phenotype was puzzling as the strain retains functional native PLY yet
361 still has reduced COMMD2 levels in comparison to wildtype TIGR4. This disparity suggested that both
362 SpxB and PLY are necessary for COMMD2 nuclear accumulation under wild type conditions. We
363 addressed the synergy between PLY and SpxB by comparing different phenotypes using exogenous
364 purified Pneumolysin toxin alone or in combination with the main byproduct of SpxB, hydrogen
365 peroxide. We first determined the IC_{50} for hydrogen peroxide and purified Pneumolysin toxin
366 individually at 28.30μM and 7.10nM, respectively, however when combined the calculated IC_{50} for
367 hydrogen peroxide dropped to 10μM (Sup. Fig. 10A & B). These results show that the combination of
368 PLY and SpxB impact cellular toxicity more than with each individual component [51].
369 We then tested the impact of exogenous supplementation of 0 – 6.25μM hydrogen peroxide
370 during challenge with either a wildtype, a TIGR4 ΔSpxB, or a TIGR4 ΔSpxBΔPly mutant strain (Sup. Fig.
371 10D – F). Our results showed increasing concentration of exogenous hydrogen peroxide resulted in
372 TIGR4ΔSpxB phenocopying wildtype except at the highest concentrations, where wildtype induced
373 more nuclear COMMD2. There was no significant increase in nuclear COMMD2 levels for either the
374 TIGR4 ΔSpxBΔPly or JW TIGR4ΔPLY W433F pore mutants against their parental wildtype strains (Sup.
375 Fig. 10E & F). Overall, these data suggest, at least for TIGR4, that PLY and hydrogen peroxide are
376 mutually synergistic in driving nuclear COMMD2 levels.
377 Capsule is another key bacterial determinant of pneumococcus and drives many virulence
378 mechanisms. We therefore tested whether capsule was required for COMMD2 nuclear translocation.

By comparing a wild type (JW TIGR4) to a capsule mutant (JW TIGR4ΔCPS), we observed no difference in their ability to induce nuclear translocation of COMMD2 (Fig. 8E).

We next assessed the association of COMMD2 nuclear localization with isolates favoring either commensal-like/carriage (6B ST138, 11A ST6521 & 19A ST276) or invasive (1 ST304 or 1 ST306 - which harbors a non-hemolytic Pneumolysin toxin) for their capacity to drive COMMD2 nuclear translocation. As expected, our results showed that invasive TIGR4 challenge significantly increased nuclear COMMD2 (pV≤ 0.0001) in comparison to the commensal-like 6B ST90 isolate and uninfected cells (Fig. 8E). Comparing the invasive serotype 1 ST304 and ST306 (non-hemolytic) isolates to TIGR4 revealed no significant differences in their capacity to induce nuclear COMMD2, whereas the commensal-like/carriage 11A ST6521 and 19A ST276 isolates resembled 6B ST90 which did not display COMMD2 localization (Fig. 8E). Interestingly, the two 6B strains, which only differ in their genomic sequence rather than their capsule, were phenotypically different in their nuclear COMMD2 levels. In contrast to 6B ST90 (Global Pneumococcal Sequence Cluster[52]; GPSC 23), 6B ST138 (GPSC 24) not only induced significantly (pV≤ 0.05) more COMMD2 translocation in comparison with the uninfected control but had an elevated level compared to 6B ST90 (pV = 0.07; Fig. 8E). Given this result, we assessed whether the elevated COMMD2 levels with 6B ST138 correlated with in vivo lethality using two challenge doses in an intranasal murine challenge model comparing 6B ST138 to TIGR4 (Fig. 8F & Sup. Fig 10G). At the high dose 6B ST138 induced lethality to a comparable level to that of TIGR4, which stands in contrast to our previously demonstrated findings that 6B ST90 was not lethal in this model even at a log higher dose to that of TIGR4 [6]. Therefore, we concluded that in a dose dependent manner challenge with 6B ST138 (GPSC 24) has higher pathogenic potential than 6B ST90 (GPSC 23), and this correlates with the differential COMMD2 nuclear signal. Overall, the combination of these data provides strong evidence that COMMD2 translocation is predominantly associated with pneumococcal virulence phenotypes both in vitro and in vivo.

Discussion:

Cellular inflammatory response is a critical component of the host defense to bacteria. Yet, the molecular processes that fine-tune cellular immunity cascades across the range of colonizing to virulent bacteria are poorly understood. We show that an invasive *S. pneumoniae* TIGR4 strain, which causes symptomatic disease in murine models [6], drives a different NF-κB p65 activation profile in comparison to a commensal-like 6B ST90 strain and IL-1β – a potent inflammatory cytokine. Our mass spectrometry interactome and post-translational modification analysis, showed these two pneumococcal isolates have diverging p65 interacting partners and phosphorylation status. Analysis of these partners demonstrated that the invasive TIGR4 strain enriched for aggrephagy pathway components and COMMD2, whereas the 6B ST90 strain did not. Through our study of COMMD2 we show that TIGR4 triggers p65 degradation and induces a unique interaction of COMMD2 with p65 and p62. By deeply investigating this process we discovered COMMD2 is a negative regulator of cellular immunity and its nuclear levels associated with invasive favoring pneumococcal isolates. Altogether, we show a bacterial pathogenesis mechanism repressing host cellular immunity through bacterial driven degradation of NF-κB p65 via novel fine-tuning of its interacting partners.

Negative regulation of NF-κB signaling, in contrast to the breadth of knowledge on activatory mechanisms, is poorly documented. This is in part due to the lack of identified targets and mechanisms responsible for attenuating this signaling cascade. Of the known negative regulators, A20 (TNAIP3) and COMMD1 are the better described with the studies using cytokine stimulation. Pointedly neither of these proteins were found in our TIGR4 p65 interactome, which suggests that COMMD2 recruitment during bacterial infection is specific. A20 is primarily a deubiquitinase whose transcription is NF-κB activation dependent. A20 functions in a negative feedback loop to deubiquintinate NEMO, which results in its stabilization with the IKK complex to restore NF-κB sequestration in the cytoplasm. This ultimately terminates the downstream canonical NF-κB signaling cascade of inflammatory response [18,25,53]. In contrast, COMMD1 transcription is NF-κB independent, and facilitates p65 termination by CRM1 mediated export and translocation of p65 to the proteasome for degradation,

while in parallel occupying the formerly p65 bound kappa-binding site at specific gene promoters [27,29,30,32,34,35 33]. It was put forth that the diversity of potential COMMD and NF-κB assemblies respond to an array of physiological stimuli to fine-tune cellular immunity positioning this family of proteins as powerful selective negative regulators of NF-κB signaling. Interestingly, our post-translational modification analysis of COMMD2 discovered a ubiquitinated peptide associated with a lysine at residue 50, which aligns with our results indicating selective degradation of COMMD2-p65-p62 complex. The COMMD2 negative feedback loop on p65 that we uncover here may represent, even in a cellular state without bacterial infection, a precise mechanism to terminate or shift a given p65 dependent transcription repertoire.

Given the vast array of post-translational modifications on p65 and other NF-κB subunits across differential stimulations has given rise to the "NF-κB barcode hypothesis", which suggests that distinct patterns are linked to how inflammatory gene transcription occurs [54,55]. Supporting this is our exploratory mass spectrometry of p65 phosphorylation, which identified serine 45 (S45) as the only enriched phosphorylated mark during TIGR4 challenge. This mark has previously been shown to negatively regulate p65, although the mechanism is unknown [56]. Lanucara et al., showed that a phosphomimetic mutant of S45 prevented IL-6 transcription and p65 binding to the IL-6 promoter after 3 hours of TNFα stimulation [56]. It remains to be evaluated how this modification affects COMMD2-p62 degradation of p65 or upon repressing p65 host transcription. Notably our previous studies showed TIGR4 challenge induces de-phosphorylation of histone H3 serine 10, which is an essential histone modification associated with inflammatory gene transcription [41,57]. Understanding how this event relates to p65 turnover and COMMD2 may shed light on essential chromatin remodeling dynamics needed to precisely regulate NF-κB p65 DNA binding, extraction and transcription termination not only to pneumococci but also under inflammatory stimuli. Excitingly, the commensal-like 6B ST90 does not induce phosphorylation of this S45 residue. Instead, this strain leads to phosphorylation on S203 in addition to S536 and S276. These marks may be critical for the upregulation of the histone demethylase KDM6B, which we previously showed was required for bacterial containment in the upper respiratory tract [6]. Future investigations here may be the best positioned to decipher outstanding questions on how bacteria engage the non-canonical NF-κB pathway and how KDM6B is selectively recruited to gene targets during bacterial infection. Whether differential phosphorylation of p65 is the determining factor in the host response to different strains of pneumococcus remains to be determined. It is tempting to speculate that posttranslational modifications of p65 may represent markers of either host response to commensal or to invasive bacteria.

To date our work is the first to show that COMMD2 mediates p65 turnover through p62 and aggrephagy, a selective form of autophagy, while simultaneously repressing host cellular immunity. TIGR4, along with other pneumococcal isolates associated with higher virulence potential, triggered COMMD2 nuclear accumulation. These findings suggest that nuclear localization of COMMD2 could be a marker of virulence, distinguishing the host response from commensal-like isolates. We show that COMMD2 nuclear translocation was independent of the TIGR4 capsule, but dependent on a tandem function of Pneumolysin (Ply) and Pyruvate oxidase (SpxB), as a ΔPly mutant shows no COMMD2 nuclear accumulation, but a ΔSpxB mutant induced partial COMMD2 translocation with a distinct phenotype. Our efforts titrating hydrogen peroxide, the product of *SpxB*, with the TIGR4 ΔSpxBΔPly or JW TIGR4ΔPLY W433F pore mutants revealed at least for TIGR4, PLY and hydrogen peroxide are mutually synergistic in driving nuclear COMMD2 levels and strongly support that Pneumolysin may be "masking" other bacterial effectors. Given the documented influence of Pneumolysin toxin, like other CDC toxins, on host plasma membrane, the known differences in Pneumolysin alleles [58], and the known role of COMMD proteins, along with CCDC22 and CCDC93 (the CCC complex), in phosphatidylinositol-3-phosphate (PI3P) equilibrium within endosomes [44] raises the possibility that combinations of Pneumolysin toxin alleles with hydrogen peroxide may alter host membrane compositions. Deeper comparative studies between pneumococcal isolates and virulence associated bacterial protein mutants may likely identify new bacterial proteins that alter host

481 response. Moreover, our comparison of two serotype 6B isolates varying in sequence type and Global
482 Pneumococcal Sequence Cluster resulted in different COMMD2 nuclear amounts which correlated
483 with increased 6B ST138 (GPSC 24) dose dependent lethality during intranasal murine challenge. Thus,
484 we propose invasive favoring pneumococcal isolates, as opposed to commensal-like ones, shape host
485 cellular immunity, and potentially disease onset and lethality, through potent shifts in host
486 transcription factor partners.
487 Tuning cellular immunity is fundamental for processes of airway epithelial cells exposed to
488 pneumococcus [7,59]. The pro-inflammatory cytokines, TNF-α and IL-1β, are major cytokines necessary
489 for neutrophil recruitment and are found in bronchoalveolar lavage fluid of animals challenged with
490 pneumococcal isolates [7,59,60]. However, a study showed that isolated murine lung epithelial cells
491 exposed to serotypes 19 and 3 failed to induce p65 (RelA) nuclear translocation in comparison to TNFα
492 and IL-1β cytokine treatment alone [7]. Indeed during respiratory infection with other microbes [61,62], a
493 balance is needed between pro-inflammatory responses and negative regulation to ensure minimal
494 tissue damage from the influx of neutrophils into the airway tissues [60]. Airway epithelial cells play a
495 crucial role in both situations by regulating neutrophil recruitment and promoting epithelial repair
496 pathways leading to tissue resilience and resolution of inflammation [59,60,63,64]. With invasive
497 pneumococci actively antagonizing the ability of airway epithelial cells to mount a cellular immune
498 response, we hypothesize an amplifying and runaway inflammatory cascade is created in latter stages
499 of infection where neutrophil influx is detrimental [59,64,65]. This could lead to exacerbated and severe
500 pneumonia with excessive tissue damage, allowing pneumococcus to transmigrate to deeper tissues.
501 We put forth that COMMD2, or combinations of COMMD proteins are modulators of bacterial driven
502 inflammatory processes and may represent a therapeutic target to circumvent collateral tissue
503 damage.
504 In conclusion, our study shows a new regulatory role for COMMD2 in restraining p65 through
505 aggrephagy mediated turnover triggered by bacterial interaction. We reveal this process to be specific
506 to invasive TIGR4 pneumococcal challenge and partially depend on pneumolysin. Further studies
507 characterizing both the p65 and COMMD2 interactome under bacterial challenge with isolates
508 representing divergent pneumococcal host interaction may identify new processes exploited at the
509 microbe-host interface to regulate cellular immunity.
510
511 **Materials and methods:**
512 Bacteria strains, growth, and enumeration. Pneumococcal isolates of 6B ST90 CC156 lineage F (ST90),
513 6B ST138, 11A ST6521, 19A ST276, 1 ST304 or 1 ST306, and TIGR4 were obtained from either the
514 Centre National de Référence des Pneumocoques (Emmanuelle Varon; Paris, France) or (Thomas
515 Kohler, Universität Greifswald) respectively. JW TIGR4 and ΔW433F pore mutants were a gift from Dr.
516 Jeffrey N. Weiser [49]. The TIGR4 ΔSpxB and TIGR4 ΔSpxBΔPly mutants were generated previously [41].
517 Experimental starters were made from master glycerol stocks struck on 5% Columbia blood agar plates
518 (Biomerieux Ref# 43041) and grown overnight at 37°C with 5% CO_2 prior to outgrowth in Todd-Hewitt
519 (BD) or Brain heart infusion (BHI) broth as previously described [6]. Inocula were prepared from frozen
520 experimental stocks grown for 3 – 4 hrs to midlog phase in BHI at 37°C with 5% CO_2 in closed falcon
521 tubes. Bacterial cultures were pelleted at 1,500xg for 10 mins at room temperature (RT), washed in
522 DPBS, and concentrated in 1mL DPBS prior to dilution at desired CFU/mL using 0.6 OD_{600} /mL
523 conversion factors in desired cell culture media [6]. Bacterial counts were determined by serial dilution
524 plating on 5% Columbia blood agar plates and grown overnight at 37°C with 5% CO_2.
525
526 Cell culture conditions and in vitro challenge. A549 human epithelial cells (ATCC ref# CCL-185) and
527 A549 stable cell lines were maintained in F12K media (Gibco) supplemented with 1x GlutaMax (Gibco)
528 and 10% heat inactivated fetal calf serum (FCS) at 37°C with 5% CO_2. Primary human nasal epithelial
529 cells (HNEpC; PromoCell ref# C-12620; lot# 475Z023) were cultured and maintained in PneumaCult™-
530 Ex Plus Medium (STEMCELL Technologies cat# 16237380). All cell lines were discarded after passage
531 4. For challenge studies cells were plated in tissue culture treated plates at $2x10^5$ cells (6well; for 72

532 hrs), $5x10^4$ cells (24well; for 48 hrs), or $1x10^4$ cells (96well; for 48 hrs) [66]. Bacterial inocula (Multiplicity
533 of infection (MOI) 20) were diluted in cell culture media, added to cells, and bacterial-epithelial cell
534 contact synchronized by centrifugation at 200xg for 10 mins at RT. Plates were moved to 37°C with
535 5% CO_2 for 2 hrs and processed as desired for experiment termination. For inhibitor studies, cell
536 culture media was aspirated, and replaced with filter sterilized culture media containing either
537 Bafilomycin A1 400 nM final concentration (Sigma ref# SML1661) or Leptomycin B 10 nM final
538 concentration (Sigma ref# L2913) for 3 hrs prior to bacterial addition. Human IL-1β (Enzo Life Sciences
539 ref# ALX-522-056) was used at 10 ng/mL final concentration in cell culture media.
540
541 RNA isolation and RT-qPCR. Total RNA isolated and extracted using TRIzol (Life technologies
542 ref#15596-026) method as per manufacturer's recommendations. Recovered RNA (5 µg) was
543 converted to cDNA with Super Script IV as per manufacturer's instructions, diluted to 20 ng/µL in
544 molecular grade water and 1 µL used for Sybr Green reactions as per manufacturer's instructions on
545 a BioRad CFX384 (BioRad). Relative expression was calculated by ΔΔCt method to *GapDH* [67] with RT-
546 PCR primers in Sup. Table 3 [6].
547
548 ChIP and ChIP-qPCR. Detailed ChIP buffer components and procedure were completed as previously
549 reported [66]. Briefly, $8x10^6$ A549 cells were cross-linked with 1% formaldehyde at room temperature
550 and quenched with 130 mM glycine. Chromatin was generated from the collected cell pellets by lysis
551 and sonication in chromatin shearing buffer to a size of 200-900bp. ChIP grade antibody to p65 (L8F6)
552 (CST ref #6956) was used at manufacturer's recommended concentrations and bound to DiaMag
553 beads (diagenode ref # C03010021-150) overnight with gentle rotation. Quantified chromatin was
554 diluted to 10 µg per immunoprecipitation and added to antibody bound DiaMag beads overnight with
555 gentle rotation and 8% of input reserved. Beads were washed as previously described [66], and DNA
556 purified using phenol-chloroform extraction followed by isopropanol precipitation. Recovered DNA
557 suspended in molecular grade water was used for Sybr Green reactions (1 µL) on a BioRad CFX384
558 (BioRad). ChIP-qPCR primers (50-150 bp; 60 °C max melt temperature) were designed to span the NF-
559 κB sites of interest within the promoters of *CFS2* or *PTGS2* [68]. % recovery was calculated as 2 raised
560 to the adjusted input Ct minus IP Ct multiplied by 100. ChIP qPCR primers listed in Sup. Table 3.
561
562 Plasmids, molecular cloning and stable cell line generation. All plasmids and primers are listed in Sup.
563 Table 3 . Routine cloning was carried out by in vivo assembly [69,70]. Briefly, primers were designed with
564 a 15-20 bp overlap to amplify nucleic acid targets using Phusion Plus polymerase (Thermo ref# F630S).
565 Correct sized bands were excised and nucleic acid extracted by "Freeze and squeeze" [71,72]. Herein,
566 0.7% - 1% agarose gel fragments were frozen for 5 mins on dry ice and centrifuged for 15 mins at
567 >21,000 xg with the supernatant collected – the process was completed two additional times.
568 Collected supernatant containing nucleic acid was then purified using phenol-chloroform extraction
569 followed by isopropanol precipitation and suspension in molecular grade water. Collected nucleic acid
570 was quantified spectrophotometrically using a NanoDrop and mixed at 3:2 (vector: insert) in 10 µl and
571 added to chemically competent E. coli MC1061 or DH5α for transformation. After 1 hr incubation on
572 ice bacteria outgrowth was done for 1 hr in Luria-Bertani (BD) prior to selection on LB agar containing
573 Ampicillin antibiotic (100 µg/mL). All plasmids were isolated with the QIAprep Spin Miniprep Kit
574 (Qiagen ref# 27106) and eluted in molecular grade water (endotoxin free) as per manufacturer's
575 instructions. A549 stable cell lines were generated using the transposon-based sleeping beauty system
576 [73,74]. A549 cells were plated in tissue culture treated plates at $2x10^5$ cells (6well) one day prior to
577 transfection with 2 µg plasmid DNA + 150 ng SB100 transposase DNA. After transfection, cells were
578 selected with 1 mg/mL Geneticin (Thermo ref# 10131035) for 7 days, with media exchanged on days
579 1, 3, 5 & 7. Cells were collected with Trypsin 0.25% EDTA (Thermo ref# 25200056) and two-way serial
580 diluted in a 96 well tissue culture plate for another 7 – 14 days with 1 mg/mL Geneticin to select
581 colonies that were phenotypically bright were mixed and expanded prior to FACS sorting to ensure
582 purity, and uniform expression.

583 Immunoblots and quantification. Whole cell lysates were obtained by RIPA lysis (10 mM Tris HCL pH
584 7.5, 150 mM EDTA, 0.1% SDS, 1% Triton X-100 & 1% Deoxycholate) supplemented with inhibitor
585 cocktail (1X PhosSTOP, 10 mM sodium butyrate, 0.2 mM PMSF). Samples combined with 5x with
586 Laemmli buffer [75], sonicated for 5 mins in a ultrasonic water bath, boiled at 98°C (dry bath) for 10 mins
587 and frozen at -20°C. Whole cell lysates were ran on 4 – 20% pre-cast polyacrylamide SDS PAGE gels
588 (BioRad), transferred to PVDF membrane (BioRad TransBlot) and blocked 1 hr in 5% BSA TBST at room
589 temperature. Membranes were probed overnight at 4°C in 5% BSA TBST with primary antibody to p65
590 (CST ref #6956 or CST ref# 8242), p65 phosphorylation at serine 536 (CST ref# 3033), p65
591 phosphorylation at serine 276 (abcam ref# ab183559), SQSTM1 / p62 antibody [EPR4844] (abcam ref#
592 ab109012) or actin AC-15 monoclonal (Sigma ref# A5441) as per manufacturer's recommendations.
593 COMMD2 immunoblots were blocked for 1 hr at room temperature in 3% milk TBST and probed
594 overnight at 4°C with the primary antibody (Sigma ref# HPA044190) suspended in 3% milk TBST.
595 Appropriate secondary-HRP conjugated antibodies in 5% Milk TBST were incubated for 1 hr at room
596 temperature prior to development with clarity ECL (BioRad) developing reagents with a ChemiDoc
597 Touch (BioRad). Band intensity was quantified by Image Lab (BioRad) with linear intensity values $\log_{10}$
598 transformed and normalized to actin prior to any additional ratio metric comparisons.
599
600 siRNA and transfection. Primary human nasal cells were seeded at $2x10^4$ cells per well in a 96well plate
601 the day before RNAi transfection. For RNAi 1 µl of 2 µM Silencer Select siRNA stock for either COMMD2
602 (Ambion ID# s27490; or Ambion ID# s27488) or SQSTM1 (p62; Ambion ID# s16961) was diluted with
603 9 µl Opti-MEM (Thermo cat# 31985062) and mixed with 10 µl of 0.003% (vol/vol) Lipofectamine
604 RNAiMAX (Thermo cat# 13778030)/ Opti-MEM. For COMMD2 siRNA mix, a final 2 µM concentration
605 of siRNA was respected. Complexes were formed during 15 min incubation at room temperature prior
606 to 20 µl of mixture added to previously seeded cells. 96well plate was incubated for an additional 72
607 hrs 37°C with 5% CO_2 prior to challenge studies.
608
609 Cell fractionation. Fractionation was performed as previously described as previously described [66].
610 Faction lysates were combined with 5x with Laemmli buffer [75], sonicated for 5 mins in a ultrasonic
611 water bath, boiled at 98°C (dry bath) for 10 mins and frozen at -20°C. Samples were ran on either 10%
612 (for GFP-COMMD2) or 12% (for fraction quality controls) polyacrylamide SDS PAGE gels (BioRad),
613 transferred to PVDF membrane (BioRad TransBlot), blocked 1 hr in 5% BSA TBST at room temperature.
614 Primary antibody in 5% BSA TBST to GFP (abcam ref# ab290), GapDH (abcam ref# ab8245), or histone
615 H4 (abcam ref# ab177840) was completed overnight at 4°C. After 3x 10 min washes in TBST
616 appropriate secondary-HRP conjugated antibodies in 5% Milk TBST were incubated for 1 hr at room
617 temperature and developed with a ChemiDoc Touch (BioRad) as described above.
618
619 Immunofluorescence microscopy and Cellprofiler analysis. For microscopy cells were seeded either on
620 acid washed and UV treated coverslips (24well) or directly in 96well plates as described above. Two
621 hours post-challenge media was aspirated, cells washed in DPBS, and fixed with 2.5% PFA for 10 mins
622 at RT. Fixed cells were blocked and permeabilized overnight in 5% BSA 0.5% Tween20 at 4°C. Primary
623 antibody to p65 (CST ref #6956 or CST ref# 8242), or p62 (SQSTM1; abcam ref# ab109012) were diluted
624 at 1:1,000 in 5% BSA 0.5% Tween20, for time course of p65 phosphorylation at serine 536 cells were
625 stained with MA5-15160 (Thermo; 1:1000), and incubated overnight at 4°C. Cells were washed 3x 10
626 mins at RT in PBS + 0.1% Tween20 prior to 1 hr incubation at 1:1,000 dilution of either Alexa Fluor 594
627 or Alexa Fluor 647 secondary antibody. Nuclei were stained with 10 ng/mL final concentration of
628 Hoechst 33342 or Draq5 for 15 mins. Coverslips were rinsed in PBS and molecular grade water prior
629 to mounting with Fluoromount-G Mounting Medium (INTERCHIM). Confocal microscopy images were
630 acquired on a Nikon TiE inverted microscope with an integrated Perfect Focus System (TI-ND6-PFS
631 Perfect Focus Unit) and a Yokogawa Confocal Spinning disk Unit (CSU-W1). Nine images per well were
632 acquired using a 20X air objective (NA 0.75) at a step-size of 0.9µm in z-plane. Deconvoluted

633 epifluorescent images were acquired on a Cytation 5 (BioTek) using a 20X air objective (NA 0.75) with
634 a grid of 3 x 3 (9 images en total).
635
636 Images were processed for background using Fiji [76], and segmented using Cell Profiler [77-79]. Briefly,
637 image analysis consisted of sequential modules to 'IdentifyPrimaryObjects' based on channel signal
638 for nuclei (Hoechst 33342 or Draq5 stain), p65 (Alexa594), or p62 (Alexa594). This was followed by
639 'IdentifySecondaryObjects' for the GFP-COMMD2 signal via propagation of identified nuclei. Objects
640 were related to each other to maintain cohesion between identified nuclei, cell and cellular contents
641 (p65 or p62). For puncta, the additional module, 'EnhanceorSupressFeatures' with 'Speckles', was
642 used. This used a global threshold strategy with Otsu threshold method and a 2% minimum boundary
643 to identify puncta contained within the segmented nuclei.
644
645 Immunoprecipitation. Cells were lysed in 250 µL of RIPA lysis (10 mM Tris HCL pH 7.5, 150 mM EDTA,
646 0.1% SDS, 1% Triton X-100 & 1% Deoxycholate) supplemented with a protease mixture inhibitor
647 (Roche Complete, EDTA free). Lysates were either immunoprecipitated using GFP-trap agarose beads
648 (ChromoTek ref# gta-10) or with DynaBeads Protein G (Thermo ref# 10004D). For GFP-p65 and GFP-
649 COMMD2 the samples were immunoprecipitated as per manufacturer's instructions with the elution
650 was recovered in either 5x with Laemmli buffer [75] and boiled at 98°C (dry bath) for 10 mins, or left in
651 Trypsin digest buffer (see LC-MS/MS Mass-spectrometry and analysis). All samples were frozen at -
652 20°C. For endogenous samples the lysates were incubated on a rotating wheel at 4 °C for 20 min before
653 adding 1 mL of dilution buffer (150 mM NaCl and 50 mM Tris-HCl pH 7.5 supplemented with Protease
654 mixture inhibitor) to reduce the detergent final concentration below 0.1%. The lysates were then
655 centrifuged at 10,000 × g for 10 min. For p65 IP the lysates were then incubated with 2 µg of antibody
656 CST ref #6956) at 4 °C overnight before adding 50 µL of Dynabeads for 1 hr. The beads were then
657 washed three times in 0.01%Tween20 PBS before adding 20 µL of Laemmli buffer supplemented with
658 2% β-mercaptoethanol and boiled for 5 min.
659
660 Exogenous Hydrogen peroxide and Pneumolysin toxin challenges. For viability studies titrations of
661 hydrogen peroxide (9 M stock, Thermo ref# 411881000; 0 µM – 240 µM) and Pneumolysin toxin
662 (50µM stock; gift Dr. T. Mitchell; final 0 nM – 50 nM), concentrations were serial diluted into cell
663 culture media. After 2 hrs of incubation samples were PFA fixed and nuclei stained with Draq5 (Thermo
664 ref# 62252) to determine viability. Bacterial challenge experimental starters of TIGR4 ΔSpxB, TIGR4
665 ΔSpxBΔPly, JW TIGR4 and ΔW433F were grown and diluted in cell culture media as in "Bacterial strains,
666 growth and enumeration". These inocula were combined with cell culture media containing indicated
667 hydrogen peroxide concentrations (0 µM – 6.25 µM) and added to cells seeded in 96 well plates. After
668 2 hrs cells were PFA fixed and COMMD2 nuclear levels determined as in "Immunofluorescence
669 microscopy and Cellprofiler analysis".
670
671 Cytokine quantification by Luminex. Supernatants we collected from primary nasal epithelial cells
672 seeded in a 96well plate as previously described. For this 200 µl of supernatant per well was collected
673 2 hrs post-challenge with IL-1β or bacteria, centrifuged in a 96well U-bottom plate for 10 min at 1,500
674 x g to pellet bacteria and cellular debris. 120 µl of cleared supernatant was collected into a 96well flat
675 bottom plate and frozen at -20°C until use. Secretion in the supernatant of 29 proteins (Human
676 Magnetic Luminex Assays, R&D Systems) was measured following manufacturer's instructions using
677 Luminex xMAP technology. Briefly, samples and standards were incubated with capture beads for 2
678 hours at RT. After washing, detection antibody mix was added and incubated for 1 hour at RT. After
679 washing, streptavidin-PE was added and incubated for 30 minutes at RT. Samples were acquired on a
680 Bioplex 200 (Biorad). Analysis was performed using the Bioplex Manager Software. Concentration of
681 each analyte was calculated using a 5-PL regression curve.
682

683 LC-MS/MS Mass-spectrometry and analysis. For label-free quantitative proteomic analysis of GFP-p65
684 and GFP-COMMD2 the respected A549 cell lines were plated in 6well tissue culture plates, and
685 challenged with bacteria for 2hrs as described above. One plate (~$5x10^7$ cells) per condition was
686 harvested using RIPA lysis and immunoperciptated with GFP-trap agarose beads (ChromoTek ref# gta-
687 10) as per manufacturer's instructions. Three or four independent biological replicates were prepared
688 and analyzed for each condition. Prior to on-bead Trypsin digestion, the samples were washed 3x in
689 trypsin digest buffer (20 mM Tris.HCl pH 8.0, 2 mM $CaCl_2$).
690
691 For pull down of GFP-p65 on bead digestion was performed strictly as described by Chromotek. Briefly,
692 beads were suspended in digestion buffer (Tris 50 mM pH 7.5, urea 2 M, 1 mM DTT and 5 µg.µl of
693 trypsin (Promega)) for 3 min at 30°C. Supernatants were transfer to new vials and beads were washed
694 twice using (Tris 50 mM pH 7.5, urea 2 M and iodoacetamide 5 mM). All washes were pulled and
695 incubated at 32°C for overnight digestion in the dark. Peptides were purified using C18 stage tips
696 protocol [80].
697
698 LC-MS/MS analysis of digested peptides was performed on an Orbitrap Q Exactive Plus mass
699 spectrometer (Thermo Fisher Scientific, Bremen) coupled to an EASY-nLC 1200 (Thermo Fisher
700 Scientific). A home-made column was used for peptide separation (C_{18} 30 cm capillary column picotip
701 silica emitter tip (75 µm diameter filled with 1.9 µm Reprosil-Pur Basic C_{18}-HD resin, (Dr. Maisch GmbH,
702 Ammerbuch-Entringen, Germany)). It was equilibrated and peptide were loaded in solvent A (0.1 %
703 FA) at 900 bars. Peptides were separated at 250 $nl.min^{-1}$. Peptides were eluted using a gradient of
704 solvent B (80% ACN, 0.1 % FA) from 3% to 31% in 45 min, 31% to 60% in 17 min, 60% to 90% in 5 min
705 (total length of the chromatographic run was 82 min including high ACN level step and column
706 regeneration). Mass spectra were acquired in data-dependent acquisition mode with the XCalibur 2.2
707 software (Thermo Fisher Scientific, Bremen) with automatic switching between MS and MS/MS scans
708 using a top 12 method. MS spectra were acquired at a resolution of 70000 (at *m/z* 400) with a target
709 value of 3×10^6 ions. The scan range was limited from 300 to 1700 *m/z*. Peptide fragmentation was
710 performed using higher-energy collision dissociation (HCD) with the energy set at 27 NCE. Intensity
711 threshold for ions selection was set at 1×10^6 ions with charge exclusion of $z = 1$ and $z > 7$. The MS/MS
712 spectra were acquired at a resolution of 17500 (at *m/z* 400). Isolation window was set at 1.6 Th.
713 Dynamic exclusion was employed within 30 s. Recorded spectra were searched with MaxQuant
714 (version 1.5.3.8) using the Andromeda search engine[81] against a human database (74368 entries,
715 downloaded from Uniprot the 27th of September 2019), a Streptococcus pneumoniae R6 database
716 (2031 entries, downloaded from Uniprot the 1st of January 2020) and a Streptococcus pneumoniae
717 serotype 4 database (2115 entries, downloaded from Uniprot 1st of January 2020).
718
719 The following search parameters were applied: carbamidomethylation of cysteines was set as a fixed
720 modification, oxidation of methionine and protein N-terminal acetylation were set as variable
721 modifications. The mass tolerances in MS and MS/MS were set to 5 ppm and 20 ppm respectively.
722 Maximum peptide charge was set to 7 and 5 amino acids were required as minimum peptide length.
723 At least 2 peptides (including 1 unique peptides) were asked to report a protein identification. A false
724 discovery rate of 1% was set up for both protein and peptide levels. iBAQ value was calculated. The
725 match between runs features was allowed for biological replicate only.
726
727 For pull down of GFP-COMMD2, washed beads were re-suspended in 150 µl digestion buffer (20 mM
728 Tris.HCl pH 8.0, 2 mM $CaCl_2$) and incubated for 4 hours with 1 µg trypsin (Promega) at 37˚C and shaking
729 at 1200 rpm. Beads were removed, another 1 µg of trypsin was added and proteins were further
730 digested overnight at 37°C , shaking at 750 rpm. Peptides were acidified with trifluoroacetic acid (TFA)
731 to lower the pH below 3 and desalted on reversed phase (RP) C18 OMIX tips (Agilent). The tips were
732 first washed 3 times with 100 µl pre-wash buffer (0.1% TFA in water/acetonitrile (ACN, 20:80, v/v))
733 and pre-equilibrated 5 times with 100 µl of wash buffer (0.1% TFA in water) before the sample was

734 loaded on the tip. After peptide binding, the tip was washed 3 times with 100 µl of wash buffer and
735 peptides were eluted twice with 100 µl elution buffer (0.1% TFA in water/ACN (40:60, v/v)). The
736 combined elutions were transferred to HPLC inserts and dried in a vacuum concentrator. The peptides
737 were re-dissolved in 20 µl loading solvent A (0.1% TFA in water/ACN (98:2, v/v)) of which 2 µl was
738 injected for LC-MS/MS analysis on an Ultimate 3000 RSLCnano system in-line connected to a Q
739 Exactive HF mass spectrometer (Thermo). Trapping was performed at 10 µl/min for 4 min in loading
740 solvent A on a 20 mm trapping column (made in-house, 100 µm internal diameter (I.D.), 5 µm beads,
741 C18 Reprosil-HD, Dr. Maisch, Germany). The peptides were separated on an in-house produced
742 column (75 µm x 250 mm), equipped with a laser pulled electrospray tip using a P-2000 Laser Based
743 Micropipette Puller (Sutter Instruments), packed in-house with ReproSil-Pur basic 1.9 µm silica
744 particles (Dr. Maisch). The column was kept at a constant temperature of 50°C. Peptides eluted using
745 a non-linear gradient reaching 33% MS solvent B (0.1% FA in water/acetonitrile (2:8, v/v)) in 60 min,
746 55% MS solvent B in 75 min and 70% MS solvent B after 90 min at a constant flow rate of 300 nl/min.
747 This was followed by a 5-minutes wash at 70% MS solvent B and re-equilibration with MS solvent A
748 (0.1% FA in water). The mass spectrometer was operated in data-dependent mode, automatically
749 switching between MS and MS/MS acquisition for the 12 most abundant ion peaks per MS spectrum.
750 Full-scan MS spectra (375-1500 m/z) were acquired at a resolution of 60,000 in the Orbitrap analyzer
751 after accumulation to a target value of 3,000,000. The 12 most intense ions above a threshold value
752 of 13,000 were isolated (isolation window of 1.5 m/z) for fragmentation at a normalized collision
753 energy of 30% after filling the trap at a target value of 100,000 for maximum 80 ms. MS/MS spectra
754 (145-2,000 m/z) were acquired at a resolution of 15,000 in the Orbitrap analyzer. The
755 polydimethylcyclosiloxane background ion at 445.120028 Da was used for internal calibration (lock
756 mass) and QCloud [82] has been used to control instrument longitudinal performance during the project.
757 Recorded spectra were searched with MaxQuant (version 2.0.3.0) using the Andromeda search engine
758 with default search settings including a false discovery rate set at 1% on PSM, peptide and protein
759 level.
760
761 Spectra were searched against the *Streptococcus pneumonia setotype 4* (TIGR4) (Taxid: 170187)
762 protein sequences in the Uniprot database (database release version of 04_2022, UP000000585),
763 containing 2,109 sequences (www.uniprot.org), the *Streptococcus pneumoniae* (Taxid: 1313) protein
764 sequences in the Uniprot database (database release version of 04_2022, UP000046310), containing
765 2,115 sequences (www.uniprot.org) and the human protein sequences in the Swiss-Prot database
766 (database release version of 2022_01, reference proteome: UP000005640), containing 20,588
767 sequences (www.uniprot.org). The mass tolerance for precursor and fragment ions was set to 4.5 and
768 20 ppm, respectively, during the main search. Enzyme specificity was set as C-terminal to arginine and
769 lysine, also allowing cleavage at proline bonds with a maximum of three missed cleavages. Variable
770 modifications were set to oxidation of methionine residues, acetylation of protein N-termini and lysine
771 residues, phosphorylation of serine, threonine and tyrosine and ubiquitination of lysine residues.
772 Matching between runs was enabled with a matching time window of 0.7 minute and an alignment
773 time window of 20 minutes. Only proteins with at least one unique or razor peptide were retained
774 leading to the identification of 2,328 proteins. Proteins were quantified by the MaxLFQ algorithm
775 integrated in the MaxQuant software. A minimum ratio count of two unique or razor peptides was
776 required for quantification.
777
778 <u>Data analysis for quantitative proteomics.</u> Quantitative analysis was based on pairwise comparison of
779 protein intensities. Values were log-transformed (log2). Reverse hits and potential contaminant were
780 removed from the analysis. Proteins with at least 2 peptides were kept for further statistics after
781 removing shared proteins from the uninfected GFP alone control. Intensity values were normalized by
782 median centering within conditions (normalized function of the R package DAPAR [83]). Remaining
783 proteins without any iBAQ value in one of both conditions have been considered as proteins
784 quantitatively present in a condition and absent in the other. They have therefore been set aside and

785 considered as differentially abundant proteins. Next, missing values were imputed using the impute.
786 MLE function of the R package imp4p (https://rdrr.io/cran/imp4p/man/imp4p-package.html).
787 Statistical testing was conducted using a limma t-test thanks to the R package limma [84]. An adaptive
788 Benjamini-Hochberg procedure was applied on the resulting p-values thanks to the function adjust.p
789 of R package cp4p[85] using the robust method described in ([86]) to estimate the proportion of true null
790 hypotheses among the set of statistical tests. The proteins associated to an adjusted p-value inferior
791 to a FDR level of 1% have been considered as significantly differentially abundant proteins.
792
793 Statistical analysis. All experiments, unless otherwise noted, were biologically repeated 3–5 times and
794 the statistical test is reported in the figure legend. Data normality was tested by Shapiro-Wilk test, and
795 appropriate parametric or non-parametric tests performed depending on result. P values calculated
796 using GraphPad Prism software and the exact values are in source data. Microscopy data obtained
797 from analysis of 3 – 5 image fields per biological replicate after being automatically acquired by the
798 microscope software to ensure unbiased sampling with the total number of analyzed cells or nuclei
799 noted in the figure legend.
800
801 **Data Availability:**
802 All data in the present study is available upon request from the corresponding authors. The mass
803 spectrometry proteomics data of GFP-p65 and GFP-COMMD2 have been deposited to the
804 ProteomeXchange Consortium via the PRIDE partner repository with the dataset identifiers
805 PXD032970 (p65) and PXD043886 (COMMD2).
806
807 **Code Availability:**
808 No custom code or software was used in the manuscript.
809
810 **Acknowledgements:**
811 We would like to thank Emmanuelle Varon and Thomas Kohler for their generous gifts of *S. pneumonie*
812 strains. We are appreciative of Pierre-Henri Commere and the Institut Pasteur, Flow Cytometry
813 Platform (Paris, France) for sorting of the COMMD2 stable cell line. Finally, we would like to thank
814 Daniel Hamaoui for his help processing blots during COVID-19 related work personnel restrictions.
815 Michael G. Connor is supported by a Springboard to Independence grant (AirwayStasis) from the
816 French Government's Investissement d'Avenir program, the Laboratoire d'Excellence ''Integrative
817 Biology of Emerging Infectious Diseases" (ANR-10-LABX-62-IBEID). Melanie A. Hamon received
818 support from the French government through the National Research Agency (ANR) as part of the
819 France 2030 program referenced "ANR-23-CHBS-0001" (ChromaBac). Work in the laboratory
820 Chromatin and infection unit (headed by Melanie A. Hamon) is supported by the Institut Pasteur, the
821 Fondation pour la Recherche Médicale (FRM- EQU202003010152), the Fondation iXCore-iXLife and
822 the Pasteur-Weizmann research fund. Sebastian Baumgarten is supported by the Institut Pasteur and
823 the European Commission (ERC-STG "PlasmoEpiRNA"). The views expressed in this article are those of
824 the authors and not necessarily those of the NIHR, or the Department of Health and Social Care. Jost
825 Enninga and Lisa Sanchez, members of Dynamics of host-pathogen interactions unit (Institut Pasteur),
826 are supported by the European Commission (ERC-CoG-Endosubvert), the ANR-HBPsensing, and are
827 members of the IBEID and Milieu Interieur LabExes. Filipe Carvalho was supported by a postdoctoral
828 grant through the "Investissement d'Avenir" as part of a French "Laboratoire d'Excellence" (LabEx)
829 research program: Integrative Biology of Emerging Infectious Diseases (ANR-10-LBX-62 IBEID). This
830 work was also supported by EPIC-XS, project number 823839, funded by the Horizon 2020 program of
831 the European Union.
832
833 **Author contributions:**
834 Conceived and designed all experiments: MGC and MAH. Performed and analyzed data for all
835 experiments: MGC with specific contributions from LS (confocal microscopy imaging); FC, MGE, & TC

(p65 mass spectrometry data, repeats for GFP & endogenous immunoprecipitations validations, analysis…); FI, SD and SB (COMMD2 mass spectrometry data, and analysis…), and CC (western blot and cell culture). MGC and TMNC conducted murine challenge models. MGC and MAH edited and reviewed the manuscript. MC and MAH supervised the research and secured funding. All authors approved the final manuscript.

Conflict of interest statement:

The authors declare no conflict of interest.

844 **Figure 1: TIGR4 p65 interactome is divergent from 6B ST90 and enriches for aggrephagy.** Mass-
845 spectrometry interactome (n=4 biological replicates per condition) of immunoprecipitated GFP-p65
846 from a stable A549 GFP-p65 cell line ($1x10^7$ cells total) 2 hrs post challenge with either 6B ST90 or
847 TIGR4 (MOI 20). A) Experimental scheme of mass-spectrometry study. B) Tabular summary of NF-kB
848 protein partners for TIGR4 and 6B in comparison to the GFP control. C-E) Volcano plots of TIGR4 vs.
849 GFP (C), 6B ST90 vs. GFP (D), and TIGR4 vs. 6B ST90 (E). Known NF-kB p65 partners in blue and general
850 significant targets in yellow. Lines represent -log10(pV) and fold-change (log2) cutoffs with targets of
851 interested denoted. F) STRING GO Ontology analysis of significant TIGR4 targets with term strength
852 and FDR. Full data in Sup. Table 1.
853
854 **Figure 2: TIGR4 engages NF-kB differently than commensal-like 6B ST90.** Immunoblot of A549 human
855 airway epithelial cells 2 hrs post-challenge with either IL-1β (10 ng/ml), TIGR4 (MOI 20) or 6B ST90
856 (MOI 20) (± IL-1β; 10 ng/ml). Whole cell lysates probed for p65, phosphorylated p65 at Serine 276,
857 phosphorylated p65 at Serine 536 or Actin. A) Representative image of immunoblot. Actin normalized
858 ratiometric B) phosphorylated p65 at Serine 5366 to total p65, C) phosphorylated p65 at Serine 276
859 to total p65, and D) total p65. Dot blot with mean (red line). One-way ANOVA with Dunnett's multiple
860 comparison post-hoc test for B & C. One-way ANOVA with Tukey's multiple comparison post-hoc test
861 for D. Intergroup comparison paired T-Test for B-D. **P ≤ 0.01, ***P ≤ 0.001, ****P ≤ 0.0001. Full
862 blots provided in Supplementary Information 1. E) Representative BioTek objective focused Zstack (10
863 µm) immunofluorescence microscopy of paraformaldehyde fixed A549 cells 2 h post-challenge with
864 either IL-1β (10 ng/ml) or TIGR4 (± IL-1β 10 ng/ml; MOI 20) stained for phosphorylated p65 S536
865 (magenta) and actin (phalloidin; gray). Scale bar = 50µm. F) Quantification of scaled (x16bit) mean
866 nuclear intensity of phosphorylated p65 S536. Dot blot of mean ± SEM with connected line over time
867 (n = 3 biological replicates; counts in Sup. Table 4). Comparisons are Paired T-Test at each time
868 indicated. * = significant; pV reported in Sup. Table 4.
869
870 **Figure 3: Blocking aggrephagy increases total COMMD2, p62 and p65.** Immunofluorescence confocal
871 microscopy of stable A549 GFP-COMMD2 cells pre-treated with Bafilomycin A1 (400nM) or DMSO for
872 3 h prior to 2 h post-challenge with either IL-1β (10 ng/ml) or TIGR4 (± IL-1β 10 ng/ml; MOI 20).
873 Representative images Sup. Fig. 4 & 5. Bar graph of mean ± STD (n = 3 biological replicates for p65 and
874 p62; n = 6 biological replicates for COMMD2; counts in Sup. Table 4). A & B) Quantified levels of total
875 or nuclear COMMD2. C & D) Quantified levels of total or nuclear p62. E & F) Quantified levels of total
876 or nuclear p65. G &) Quantified area (pixels) of total p65 puncta or p62 puncta (n = 3 biological
877 replicates for p65 and p62). For G & H Tukey box and whisker plot with defined box boundaries being
878 the upper and lower interquartile range (IQR), whiskers' (fences) being ± 1.5 times IQR and the median
879 depicted by the middle solid line. Dots represent outliers. One-way ANOVA with Tukey's multiple
880 comparison post-hoc test for A - H. **P ≤ 0.01, ***P ≤ 0.001, ****P ≤ 0.0001.
881
882 **Figure 4: TIGR4 challenge induces formation of a COMMD2 – p65 – p62 complex.** GFP-Trap agarose
883 immunoprecipitants were collected from a stable A549 GFP-COMMD2 cell line 2 hrs post-challenge
884 with either IL-1β (10 ng/ml) or TIGR4 (MOI 20) or 6B ST90 (MOI 20) (± IL-1β; 10 ng/ml). A & B)
885 Representative immunoblot from 3 biological replicates of GFP-COMMD2 immunoprecipitation
886 lysates (input & IP) probed for p65, p62 or GFP for COMMD2. Full blots provided in Supplementary
887 Information 1.
888
889 **Figure 5: COMMD2-p65-p62 is exported from nucleus through CRM1.** Representative
890 immunofluorescence confocal microscopy of stable A549 GFP-COMMD2 pretreated for 3 hrs with
891 Leptomycin B (10 nM) prior to 2 hr challenge with either IL-1β (10 ng/ml) or TIGR4 (MOI 20).

892 Paraformaldehyde fixed cells stained for A) p62 (magenta), or B) p65 (cyan) against GFP-COMMD2
893 (gray). Scale bar = 100 µm or 10 µm for single nuclei inserts. C & D) Co-association of intensity peaks
894 across a 20 µm segment (white line) for p62 (magenta) or p65 (cyan) to COMMD2 (black). E-G)
895 Quantified nuclear intensity of COMMD2 (E), p62 (F), p65 (G) from untreated uninfected, IL-1β or
896 TIGR4 conditions to Leptomycin B treatment. Graphed as mean ± STD with dots representing biological
897 replicates. Intergroup comparisons paired T.Test. *P ≤ 0.05, **P ≤ 0.01, ****P ≤ 0.0001.
898
899 **Figure 6: TIGR4 driven COMMD2 interactome is unique in comparison to 6B ST90 or IL-1β.** Mass-
900 spectrometry interactome (n=2 biological replicates per condition) of immunoprecipitated GFP-
901 COMMD2 from a stable A549 GFP-COMMD2 cell line ($1x10^7$ cells total) 2 hrs post challenge with either
902 TIGR4 (MOI 20), 6B ST90 (MOI 20) or IL-1β (10 ng/ml). A) Experimental scheme of mass-spectrometry
903 study. B – D) Volcano plots of TIGR4 vs. GFP-COMMD2 (B), 6B ST90 vs. GFP-COMMD2 (C), and IL-1β
904 vs. GFP-COMMD2 (D). Identified interacting partners with known NF-kB p65 interaction in blue and
905 significant targets in yellow. Lines represent -log10(pV) and fold-change cutoffs with targets of
906 interested denoted. E) Venn diagram describing the numbers of unique and shared significant proteins
907 and their total % from the mass-spectrometry dataset. Table breakdown of identified partners that
908 were significant, of the significant targets that are unique, and of the significant targets shared with
909 the p65 interactome. F) Panther classification analysis of protein class of identified COMMD2
910 interactors unique to TIGR4, shared between TIGR4 and 6B ST90, or unique to 6B ST90.
911
912 **Figure 7: COMMD2 RNAi selectively elevates host analytes associated with cellular immunity.** A)
913 Secreted analytes (Luminex) at 4 hrs from RNAi COMMD2 primary nasal cells normalized to scrambled
914 controls (n=3 biological replicates). Cells were challenged with either IL-1β (10 ng/ml) or TIGR4 (MOI
915 20) ± IL-1β (10 ng/ml). Individual p values shown in comparison to respected Scr control. Calculated
916 by unpaired T. Test. B) Absolute difference of COMMD2 RNAi to scramble control for all analytes. Dot
917 blot with mean (bars). Wilcoxon matched pairs signed rank test to TIGR4. ns = not significant, *P ≤
918 0.05, ****P ≤ 0.0001. C) Difference of either RNAi COMMD2 or p62 against scramble control for TIGR4
919 and 6B ST90. Before-after line graph. Wilcoxon matched-pairs signed rank test to TIGR4. *P ≤ 0.05,
920 **P ≤ 0.01,***P ≤ 0.001, ****P ≤ 0.0001. D) Transcription factor Affinity Prediction (TRAP) analysis [47]
921 of predicted NF-kB binding motifs ± 2kb of indicated gene TSS. Scale bar represents predicted affinity
922 score color coded. E) Weblogo [48] visual of nucleotide probability of CMD2 target genes in comparison
923 to canonical JASPAR NF-kB motif and all targets. Full details of analysis in Sup. Table 4.
924
925 **Figure 8: Invasive favoring pneumococcal isolates drive COMMD2 nuclear localization.** A)
926 Immunofluorescence deconvolution epifluorescence microscopy of A549 GFP-COMMD2 (gray) cells 2
927 hr post-challenge with either IL-1β (10 ng/ml), or MOI 20 for each bacterial strain 6B ST90, 6B ST138,
928 11A ST6521, 19A ST276, 1 ST304, 1 ST306, JW TIGR4 (JW parental wildtype), JW TIGR4 Δ*cps*, JW TIGR4
929 Δ*ply* W433F, TIGR4 (parental wildtype), TIGR4 *ΔspxB* or TIGR4 *Δply*. Relevant bacterial strain
930 information for favoring carriage or invasive host states along with mutant genotypes. Scale bar =
931 50µm. B-E) Bar graph of mean ± STD quantification of nuclear GFP-COMMD2 normalized to the
932 segmented nuclei using DAPI signal (omitted in representative images for clarity; B,D & E n = 3
933 biological replicates; C n = 6 biological replicates; counts in Sup. Table 4). One-way ANOVA with Tukey's
934 multiple comparison post-hoc test for A - H. **P ≤ 0.01, ***P ≤ 0.001, ****P ≤ 0.0001. F) C57B6 mice
935 (8-9weeks) were intranasally challenged with TIGR4 (3 - $4x10^6$ CFU; n=3), 6B ST138 (3 - $4x10^6$ CFU;
936 n=6), or 6B ST138 (3 - $4x10^7$ CFU; n=6). Survival monitored for 14 days post-infection. Kaplan-Meier
937 percent survival curve with Holm-Šídák's multiple comparisons test. **P ≤ 0.01. # = single animal
938 survived.

939 **Sup. Figure 1: Individual GO biological process enrichment for TIGR4 and 6B ST90 p65 interactomes.**
940 A-B) TIGR4 or 6B ST90 enrichment over GFP. Lollipop graph indicating FDR by color scale and number
941 of proteins by lollipop size.
942
943 **Sup. Figure 2: TIGR4 drives disparity in NF-kB gene expression and chromatin binding.** A-B)
944 phosphorylated p65 at Serine 536 or Serine 276 to actin. C) Immunoblot of primary nasal whole cell
945 lysates 2 hrs post-challenge with either IL-1β (10 ng/ml), TIGR4 (MOI 20) or 6B ST90 (MOI 20) (± IL-1β;
946 10 ng/ml) probed for phosphorylated p65 at Serine 536 and actin (n=3 biological). A – C) Dot blot with
947 mean (red line). One-way ANOVA with Dunnett's multiple comparison post-hoc test. Intergroup
948 comparison paired T-Test. **P ≤ 0.01, ***P ≤ 0.001, ****P ≤ 0.0001. Full blots provided in
949 Supplementary Information 1. D-E) Inflammatory gene transcription profiles by RT-qPCR for PTGS2 &
950 CSF2 of A549 cells over a 2 hr time course with either IL-1β or TIGR4 (± IL-1β 10 ng/ml; MOI 20).
951 Graphed as the relative expression of each indicated transcript to matched uninfected/unstimulated
952 control per time point (n = 3 biological replicates; 2 technicals per replicate). Displayed as a dot plot
953 with each data point and a bar representing the mean. Statistics table reporting significance calculated
954 by unpaired T.Test at each time point indicated. * = significant; full details of analysis in Sup. Table 4.
955 F) Schematic representation of PTGS2 or CSF2 promoter with ChIP-qPCR primer locations and NF-κB
956 sites denoted as predicted by Alibaba2-curated eukaryotic transcription factor DNA-binding motifs
957 from the TRANSFAC database [68]. G-H) 10μg chromatin input from A549 cells either untreated (light
958 gray), IL-1β treated (10 ng/ml; dark gray) or 2 hrs post-challenge with TIGR4 (± IL-1β; 10 ng/ml; MOI
959 20; light blue or dark blue respectively). ChIP-qPCR represented as % recovery against input of p65 at
960 indicated NF-κB sites. Tukey box and whisker plot with defined box boundaries being the upper and
961 lower interquartile range (IQR), 'whiskers' (fences) being ± 1.5 times IQR and the median depicted by
962 the middle solid line (n=3 biological replicates with 2 or 3 technicals per replicate). One-way ANOVA
963 comparing all means with Tukey's multiple comparison post-hoc test. ns=not significant, ****P ≤
964 0.0001.
965
966 **Sup. Figure 3: Proteasomal degradation is not involved in TIGR4 mediated p65 turnover.** Cell
967 fractions from a stable A549 GFP-COMMD2 cell line 2 hrs post-challenge with either IL-1β (10 ng/ml),
968 TIGR4 (MOI 20) or 6B ST90 (MOI 20). A) Representative immunoblot of cell fractions probed for GFP
969 (COMMD2) enrichment across cellular compartments with GapDH (cytoplasm control) or H4 (nuclear
970 control). B) Quantified nuclear COMMD2 (n = 3 biological). Bar graph with dots representing
971 experiments. One-way ANOVA with Tukey's multiple comparison post-hoc test. ns = not significant,
972 ****P ≤ 0.0001. C) Representative immunoblot of cell fractions and coomassie stained PVDF
973 membrane.
974
975 **Sup. Figure 4: Representative images of COMMD2 & p65 with Bafilomycin A1.** Representative
976 confocal microscopy images. Puncta analysis of area in pixels highlighted with color scale.
977
978 **Sup. Figure 5: Representative images of COMMD2 & p62 with Bafilomycin A1.** Representative
979 confocal microscopy images. Puncta analysis of area in pixels highlighted with color scale.
980
981 **Sup. Figure 6: TIGR4 induces endogenous COMMD2-p65 complex.** A) Representative immunoblot of
982 p65 immunoprecipitation from primary nasal cells 2 hr post-challenge with either TIGR4 or 6B ST90
983 (MOI 20; n= 4 biological). B-D) Quantified ratio of p65 to COMMD2 (prey :: bait) normalized to
984 uninfected (B), target COMMD2 ratio to uninfected normalized to input (C) and bait p65 ratio to
985 uninfected normalized to input (D). Dot and bar graph. (B) Kruskal-Wallis test with Dunn's multiple

comparison test. C-D) One-way ANOVA with Bonferroni's multiple comparison post-hoc test. *P ≤ 0.05.

Sup. Figure 7: CRM1 inhibition increases p62 puncta. A) Representative immunofluorescence confocal microscopy of stable A549 GFP-COMMD2 pretreated for 3 hrs with Leptomycin B (10 nM) prior to 2 hr challenge with either IL-1β (10 ng/ml) or TIGR4 ± IL-1β (MOI 20). Paraformaldehyde fixed cells stained for p62 (magenta) against GFP-COMMD2 (gray) and nuclei (DAPI; n=3 biological replicates; nuclei counts for Uninfected n=1041, IL-1β n=831, TIGR4 n=1164, TIGR4 + IL-1β n=1269). Scale bar = 10 µm. B) Nuclear p62 puncta average counts per cell. Graphed as mean with dots representing individual experiments. One-way ANOVA comparing all means with Tukey's multiple comparison post-hoc test. ns=not significant, *P ≤ 0.05, **P ≤ 0.01, ****P ≤ 0.0001.

Sup. Figure 8: GFP-COMMD2 vs. GFP volcano plot. Mass-spectrometry interactome (n=2 biological replicates per condition) of immunoprecipitated GFP-COMMD2 from a stable A549 GFP-COMMD2 cell line ($1x10^7$ cells total) or GFP A549 cell line control ($1x10^7$ cells total). Volcano plot of GFP-COMMD2 vs. GFP alone control. Identified interacting partners with known NF-kB p65 interaction in blue and significant targets in yellow. Lines represent -log10(pV) and fold-change cutoffs with targets of interested denoted.

Sup. Figure 9: RNAi efficiency in primary nasal cells and Luminex analyte analysis of p62 RNAi. A) Representative immunoblot of RNAi conditions targeting COMMD2 or p62 in primary human nasal epithelial cells from whole cell lysates at 48 hrs of RNAi. PVDF membrane probed for either COMMD2 or p62 protein levels. B & C) Quantification of COMMD2 and p62 protein levels post RNAi. Dot blot with mean (bars) ± STD. One-way matched ANOVA with Dunnett's multiple comparison post-hoc test comparing RNAi conditions to scrambled control. ns = not significant, **P ≤ 0.01, ***P ≤ 0.001. D) Secreted analytes (Luminex) at 4 hrs from Scr control in primary nasal cells (n=3 biological replicates) challenged with either IL-1β (10 ng/ml), TIGR4 (MOI 20) ± IL-1β or 6B ST90 (MOI 20) ± IL-1β. E) Luminex of secreted analytes at 4 hrs from RNAi p62 in primary nasal cells normalized to scrambled controls (n=3 biological replicates). Cells were challenged with either IL-1β (10 ng/ml), TIGR4 (MOI 20) ± IL-1β or 6B ST90 (MOI 20) ± IL-1β. Individual p values shown in comparison to respected Scr control. Calculated by unpaired T. Test. Full details of analysis in Sup. Table 4.

Sup. Figure 10: CMD2 nuclear translocation screen with pneumococcal mutants and hydrogen peroxide. A-C) Titration of hydrogen peroxide (A), purified Pneumolysin toxin (B), or their combination (C) upon viability of the GFP-COMMD2 A549 stable cell line (n=4 biological replicates). Graphed as a dot ± STD of biological replicates for IC_{50} calculations by 4 parameter variable slope curve (red) with IC_{50} denoted in purple dashed line. Tabular comparison of IC_{50}. D) Representative deconvolution epifluorescence microscopy of A549 GFP-COMMD2 (gray) cells 2 hr post-challenge with either MOI 20 for each bacterial strain JW TIGR4 (wildtype), JW TIGR4 Δ*ply* W433F, TIGR4 (wildtype), TIGR4 *ΔspxB* or TIGR4 *ΔspxBΔply* under titrated hydrogen peroxide treatment (0 – 6.25µM). E-F) Graphed as Dot blot with mean (bars) ± STD. One-way matched ANOVA comparing selected columns with Bonferroni's multiple comparison post-hoc test. ns = not significant, *P ≤ 0.05, **P ≤ 0.01, ***P ≤ 0.001, ****P ≤ 0.0001. G) Inocula of intranasal mouse challenge shown as bar graph of mean ± STD. One-way ANOVA comparing all means with Tukey's multiple comparison post-hoc test. ns=not significant, **P ≤ 0.01.

1030 **References**

1031 1 Myszor, I. T. & Gudmundsson, G. H. Modulation of innate immunity in airway epithelium for
1032 host-directed therapy. *Frontiers in immunology* **14** (2023).
1033 https://doi.org/10.3389/fimmu.2023.1197908
1034 2 Hewitt, R. J. & Lloyd, C. M. Regulation of immune responses by the airway epithelial cell
1035 landscape. *Nature Reviews Immunology* **21**, 347–362 (2021). https://doi.org/10.1038/s41577-
1036 020-00477-9
1037 3 Connor, M. G. & Hamon, M. A. Advances in regulation of homeostasis through chromatin
1038 modifications by airway commensals. *Current opinion in microbiology* **80**, 102505 (2024).
1039 https://doi.org/https://doi.org/10.1016/j.mib.2024.102505
1040 4 Bosch, A. A., Biesbroek, G., Trzcinski, K., Sanders, E. A. & Bogaert, D. Viral and bacterial
1041 interactions in the upper respiratory tract. *PLoS pathogens* **9**, e1003057 (2013).
1042 https://doi.org/10.1371/journal.ppat.1003057
1043 5 Hakansson, A. P., Orihuela, C. J. & Bogaert, D. Bacterial-Host Interactions: Physiology and
1044 Pathophysiology of Respiratory Infection. *Physiological reviews* **98**, 781–811 (2018).
1045 https://doi.org/10.1152/physrev.00040.2016
1046 6 Connor, M. G. *et al.* The histone demethylase KDM6B fine-tunes the host response to
1047 Streptococcus pneumoniae. *Nat Microbiol* **6**, 257–269 (2021).
1048 https://doi.org/10.1038/s41564-020-00805-8
1049 7 Quinton, L. J. *et al.* Functions and regulation of NF-kappaB RelA during pneumococcal
1050 pneumonia. *Journal of immunology (Baltimore, Md. : 1950)* **178**, 1896–1903 (2007).
1051 https://doi.org/10.4049/jimmunol.178.3.1896
1052 8 Ferreira, D. M. *et al.* Controlled human infection and rechallenge with Streptococcus
1053 pneumoniae reveals the protective efficacy of carriage in healthy adults. *American journal of*
1054 *respiratory and critical care medicine* **187**, 855–864 (2013).
1055 https://doi.org/10.1164/rccm.201212-2277OC
1056 9 Henriques-Normark, B. & Tuomanen, E. I. The Pneumococcus: Epidemiology, Microbiology,
1057 and Pathogenesis. *Cold Spring Harbor perspectives in medicine* **3**, a010215 (2013).
1058 https://doi.org/10.1101/cshperspect.a010215
1059 10 Jochems, S. P., Weiser, J. N., Malley, R. & Ferreira, D. M. The immunological mechanisms that
1060 control pneumococcal carriage. *PLoS pathogens* **13**, e1006665–e1006665 (2017).
1061 https://doi.org/10.1371/journal.ppat.1006665
1062 11 Robson, R. L., Reed, N. A. & Horvat, R. T. Differential activation of inflammatory pathways in
1063 A549 type II pneumocytes by Streptococcus pneumoniae strains with different adherence
1064 properties. *BMC Infect Dis* **6**, 71 (2006). https://doi.org/10.1186/1471-2334-6-71
1065 12 Weight, C. M. *et al.* Microinvasion by Streptococcus pneumoniae induces epithelial innate
1066 immunity during colonisation at the human mucosal surface. *Nature communications* **10**,
1067 3060 (2019). https://doi.org/10.1038/s41467-019-11005-2
1068 13 Ghosh, S. & Hayden, M. S. New regulators of NF-kappaB in inflammation. *Nature reviews.*
1069 *Immunology* **8**, 837–848 (2008). https://doi.org/10.1038/nri2423
1070 14 Bhatt, D. & Ghosh, S. Regulation of the NF-kappaB-Mediated Transcription of Inflammatory
1071 Genes. *Frontiers in immunology* **5**, 71 (2014). https://doi.org/10.3389/fimmu.2014.00071
1072 15 Rahman, M. M. & McFadden, G. Modulation of NF-κB signalling by microbial pathogens.
1073 *Nature Reviews Microbiology* **9**, 291–306 (2011). https://doi.org/10.1038/nrmicro2539
1074 16 Johannessen, M., Askarian, F., Sangvik, M. & Sollid, J. E. Bacterial interference with canonical
1075 NFκB signalling. *Microbiology (Reading, England)* **159**, 2001–2013 (2013).
1076 https://doi.org/10.1099/mic.0.069369-0
1077 17 Brücher, B., Lang, F. & Jamall, I. NF-kB signaling and crosstalk during carcinogenesis. *4open* **2**,
1078 1–35 (2019). https://doi.org/10.1051/fopen/2019010
1079 18 Hoffmann, A., Natoli, G. & Ghosh, G. Transcriptional regulation via the NF-κB signaling module.
1080 *Oncogene* **25**, 6706–6716 (2006). https://doi.org/10.1038/sj.onc.1209933

1081 19 Basak, S. & Hoffmann, A. Crosstalk via the NF-kappaB signaling system. *Cytokine & growth*
1082 *factor reviews* **19**, 187–197 (2008). https://doi.org/10.1016/j.cytogfr.2008.04.005
1083 20 Shih, V. F.-S., Tsui, R., Caldwell, A. & Hoffmann, A. A single NFκB system for both canonical and
1084 non-canonical signaling. *Cell research* **21**, 86–102 (2011). https://doi.org/10.1038/cr.2010.161
1085 21 Huxford, T. & Ghosh, G. A structural guide to proteins of the NF-kappaB signaling module. *Cold*
1086 *Spring Harbor perspectives in biology* **1**, a000075 (2009).
1087 https://doi.org/10.1101/cshperspect.a000075
1088 22 Wong, D. *et al.* Extensive characterization of NF-κB binding uncovers non-canonical motifs and
1089 advances the interpretation of genetic functional traits. *Genome biology* **12**, R70–R70 (2011).
1090 https://doi.org/10.1186/gb-2011-12-7-r70
1091 23 Christian, F., Smith, E. L. & Carmody, R. J. The Regulation of NF-κB Subunits by
1092 Phosphorylation. *Cells* **5**, 12 (2016). https://doi.org/10.3390/cells5010012
1093 24 Oeckinghaus, A. & Ghosh, S. The NF-κB Family of Transcription Factors and Its Regulation. *Cold*
1094 *Spring Harbor perspectives in biology* **1**, a000034 (2009).
1095 https://doi.org/10.1101/cshperspect.a000034
1096 25 Bartuzi, P., Hofker, M. H. & van de Sluis, B. Tuning NF-κB activity: A touch of COMMD proteins.
1097 *Biochimica et Biophysica Acta (BBA) - Molecular Basis of Disease* **1832**, 2315–2321 (2013).
1098 https://doi.org/https://doi.org/10.1016/j.bbadis.2013.09.014
1099 26 Newton, K. & Dixit, V. M. Signaling in innate immunity and inflammation. *Cold Spring Harbor*
1100 *perspectives in biology* **4** (2012). https://doi.org/10.1101/cshperspect.a006049
1101 27 Burstein, E. *et al.* COMMD proteins, a novel family of structural and functional homologs of
1102 MURR1. *The Journal of biological chemistry* **280**, 22222–22232 (2005).
1103 https://doi.org/10.1074/jbc.M501928200
1104 28 de Bie, P. *et al.* Characterization of COMMD protein-protein interactions in NF-kappaB
1105 signalling. *The Biochemical journal* **398**, 63–71 (2006). https://doi.org/10.1042/BJ20051664
1106 29 Maine, G. N., Mao, X., Komarck, C. M. & Burstein, E. COMMD1 promotes the ubiquitination of
1107 NF-kappaB subunits through a cullin-containing ubiquitin ligase. *The EMBO journal* **26**, 436–
1108 447 (2007). https://doi.org/10.1038/sj.emboj.7601489
1109 30 Maine, G. N. & Burstein, E. COMMD proteins and the control of the NF kappa B pathway. *Cell*
1110 *Cycle* **6**, 672–676 (2007). https://doi.org/10.4161/cc.6.6.3989
1111 31 Maine, G. N. & Burstein, E. COMMD proteins: COMMing to the scene. *Cellular and molecular*
1112 *life sciences : CMLS* **64**, 1997–2005 (2007). https://doi.org/10.1007/s00018-007-7078-y
1113 32 Riera-Romo, M. COMMD1: A Multifunctional Regulatory Protein. *Journal of cellular*
1114 *biochemistry* **119**, 34–51 (2018). https://doi.org/10.1002/jcb.26151
1115 33 Geng, H., Wittwer, T., Dittrich-Breiholz, O., Kracht, M. & Schmitz, M. L. Phosphorylation of NF-
1116 kappaB p65 at Ser468 controls its COMMD1-dependent ubiquitination and target gene-
1117 specific proteasomal elimination. *EMBO reports* **10**, 381–386 (2009).
1118 https://doi.org/10.1038/embor.2009.10
1119 34 Thoms, H. C. *et al.* Nucleolar Targeting of RelA(p65) Is Regulated by COMMD1-Dependent
1120 Ubiquitination. *Cancer research* **70**, 139–149 (2010). https://doi.org/10.1158/0008-5472.Can-
1121 09-1397
1122 35 Mao, X. *et al.* COMMD1 (copper metabolism MURR1 domain-containing protein 1) regulates
1123 Cullin RING ligases by preventing CAND1 (Cullin-associated Nedd8-dissociated protein 1)
1124 binding. *The Journal of biological chemistry* **286**, 32355–32365 (2011).
1125 https://doi.org/10.1074/jbc.M111.278408
1126 36 Kim, S. *et al.* Stress-induced NEDDylation promotes cytosolic protein aggregation through
1127 HDAC6 in a p62-dependent manner. *iScience* **24**, 102146 (2021).
1128 https://doi.org/https://doi.org/10.1016/j.isci.2021.102146
1129 37 Lamark, T. & Johansen, T. Aggrephagy: Selective Disposal of Protein Aggregates by
1130 Macroautophagy. *International Journal of Cell Biology* **2012**, 736905 (2012).
1131 https://doi.org/10.1155/2012/736905

1132 38 Svenning, S. & Johansen, T. Selective autophagy. *Essays in biochemistry* **55**, 79–92 (2013).
1133 https://doi.org/10.1042/bse0550079
1134 39 Lobb, I. T. *et al.* A Role for the Autophagic Receptor, SQSTM1/p62, in Trafficking NF-κB/RelA
1135 to Nucleolar Aggresomes. *Molecular Cancer Research* **19**, 274 (2021).
1136 https://doi.org/10.1158/1541-7786.MCR-20-0336
1137 40 Vonk, W. I. M. *et al.* The Copper Metabolism MURR1 Domain Protein 1 (COMMD1) Modulates
1138 the Aggregation of Misfolded Protein Species in a Client-Specific Manner. *PloS one* **9**, e92408
1139 (2014). https://doi.org/10.1371/journal.pone.0092408
1140 41 Dong, W. *et al.* Streptococcus pneumoniae Infection Promotes Histone H3 Dephosphorylation
1141 by Modulating Host PP1 Phosphatase. *Cell reports* **30**, 4016–4026.e4014 (2020).
1142 https://doi.org/https://doi.org/10.1016/j.celrep.2020.02.116
1143 42 Muller, P. A. *et al.* Nuclear-cytosolic transport of COMMD1 regulates NF-kappaB and HIF-1
1144 activity. *Traffic* **10**, 514–527 (2009). https://doi.org/10.1111/j.1600-0854.2009.00892.x
1145 43 Kudo, N. *et al.* Leptomycin B inactivates CRM1/exportin 1 by covalent modification at a
1146 cysteine residue in the central conserved region. *Proceedings of the National Academy of*
1147 *Sciences of the United States of America* **96**, 9112–9117 (1999).
1148 https://doi.org/10.1073/pnas.96.16.9112
1149 44 Singla, A. *et al.* Endosomal PI(3)P regulation by the COMMD/CCDC22/CCDC93 (CCC) complex
1150 controls membrane protein recycling. *Nature communications* **10**, 4271 (2019).
1151 https://doi.org/10.1038/s41467-019-12221-6
1152 45 You, G. *et al.* COMMD proteins function and their regulating roles in tumors. *Frontiers in*
1153 *oncology* **13** (2023). https://doi.org/10.3389/fonc.2023.1067234
1154 46 Healy, M. D. *et al.* Structure of the endosomal Commander complex linked to Ritscher-Schinzel
1155 syndrome. *Cell* **186**, 2219–2237.e2229 (2023). https://doi.org/10.1016/j.cell.2023.04.003
1156 47 Thomas-Chollier, M. *et al.* Transcription factor binding predictions using TRAP for the analysis
1157 of ChIP-seq data and regulatory SNPs. *Nature protocols* **6**, 1860–1869 (2011).
1158 https://doi.org/10.1038/nprot.2011.409
1159 48 Crooks, G. E., Hon, G., Chandonia, J. M. & Brenner, S. E. WebLogo: a sequence logo generator.
1160 *Genome research* **14**, 1188–1190 (2004). https://doi.org/10.1101/gr.849004
1161 49 Zafar, M. A., Wang, Y., Hamaguchi, S. & Weiser, J. N. Host-to-Host Transmission of
1162 Streptococcus pneumoniae Is Driven by Its Inflammatory Toxin, Pneumolysin. *Cell host &*
1163 *microbe* **21**, 73–83 (2017). https://doi.org/10.1016/j.chom.2016.12.005
1164 50 Rossjohn, J. *et al.* The molecular mechanism of pneumolysin, a virulence factor from
1165 Streptococcus pneumoniae. *Journal of molecular biology* **284**, 449–461 (1998).
1166 https://doi.org/10.1006/jmbi.1998.2167
1167 51 Bryant, J. C. *et al.* Pyruvate oxidase of Streptococcus pneumoniae contributes to pneumolysin
1168 release. *BMC microbiology* **16**, 271 (2016). https://doi.org/10.1186/s12866-016-0881-6
1169 52 Gladstone, R. A. *et al.* International genomic definition of pneumococcal lineages, to
1170 contextualise disease, antibiotic resistance and vaccine impact. *EBioMedicine* **43**, 338–346
1171 (2019). https://doi.org/10.1016/j.ebiom.2019.04.021
1172 53 Das, T., Chen, Z., Hendriks, R. W. & Kool, M. A20/Tumor Necrosis Factor α-Induced Protein 3
1173 in Immune Cells Controls Development of Autoinflammation and Autoimmunity: Lessons from
1174 Mouse Models. *Frontiers in immunology* **9** (2018).
1175 https://doi.org/10.3389/fimmu.2018.00104
1176 54 Moreno, R., Sobotzik, J.-M., Schultz, C. & Schmitz, M. L. Specification of the NF-κB
1177 transcriptional response by p65 phosphorylation and TNF-induced nuclear translocation of
1178 IKKε. *Nucleic acids research* **38**, 6029–6044 (2010). https://doi.org/10.1093/nar/gkq439
1179 55 Collins, P. E., Mitxitorena, I. & Carmody, R. J. The Ubiquitination of NF-κB Subunits in the
1180 Control of Transcription. *Cells* **5**, 23 (2016). https://doi.org/10.3390/cells5020023

56 Lanucara, F. *et al.* Dynamic phosphorylation of RelA on Ser42 and Ser45 in response to TNFalpha stimulation regulates DNA binding and transcription. *Open Biol* **6** (2016). https://doi.org/10.1098/rsob.160055

57 Saccani, S., Pantano, S. & Natoli, G. p38-Dependent marking of inflammatory genes for increased NF-kappa B recruitment. *Nature immunology* **3**, 69–75 (2002). https://doi.org/10.1038/ni748

58 Jefferies, J. M. *et al.* Identification of novel pneumolysin alleles from paediatric carriage isolates of Streptococcus pneumoniae. *Journal of medical microbiology* **59**, 808–814 (2010). https://doi.org/10.1099/jmm.0.018663-0

59 Quinton, L. J. & Mizgerd, J. P. Dynamics of lung defense in pneumonia: resistance, resilience, and remodeling. *Annual review of physiology* **77**, 407–430 (2015). https://doi.org/10.1146/annurev-physiol-021014-071937

60 Pechous, R. D. With Friends Like These: The Complex Role of Neutrophils in the Progression of Severe Pneumonia. *Frontiers in cellular and infection microbiology* **7**, 160–160 (2017). https://doi.org/10.3389/fcimb.2017.00160

61 Liu, J. *et al.* Advanced Role of Neutrophils in Common Respiratory Diseases. *Journal of immunology research* **2017**, 6710278 (2017). https://doi.org/10.1155/2017/6710278

62 Craig, A., Mai, J., Cai, S. & Jeyaseelan, S. Neutrophil Recruitment to the Lungs during Bacterial Pneumonia. *Infection and immunity* **77**, 568–575 (2009). https://doi.org/10.1128/IAI.00832-08

63 Pechous, R. D., Sivaraman, V., Stasulli, N. M. & Goldman, W. E. Pneumonic Plague: The Darker Side of Yersinia pestis. *Trends in microbiology* (2015). https://doi.org/10.1016/j.tim.2015.11.008

64 Yamamoto, K. *et al.* Roles of lung epithelium in neutrophil recruitment during pneumococcal pneumonia. *American journal of respiratory cell and molecular biology* **50**, 253–262 (2014). https://doi.org/10.1165/rcmb.2013-0114OC

65 Bou Ghanem, E. N. *et al.* Extracellular Adenosine Protects against Streptococcus pneumoniae Lung Infection by Regulating Pulmonary Neutrophil Recruitment. *PLoS pathogens* **11**, e1005126 (2015). https://doi.org/10.1371/journal.ppat.1005126

66 Connor, M. G. *et al.* The histone demethylase KDM6B fine-tunes the host response to Streptococcus pneumoniae. *Nature Microbiology* (2020). https://doi.org/10.1038/s41564-020-00805-8

67 Livak, K. J. & Schmittgen, T. D. Analysis of relative gene expression data using real-time quantitative PCR and the 2(-Delta Delta C(T)) Method. *Methods (San Diego, Calif.)* **25**, 402–408 (2001). https://doi.org/10.1006/meth.2001.1262

68 Nguyen, L. K., Cavadas, M. A. S., Kholodenko, B. N., Frank, T. D. & Cheong, A. Species differential regulation of COX2 can be described by an NFκB-dependent logic AND gate. *Cellular and molecular life sciences : CMLS* **72**, 2431–2443 (2015). https://doi.org/10.1007/s00018-015-1850-1

69 Huang, F., Spangler, J. R. & Huang, A. Y. In vivo cloning of up to 16 kb plasmids in E. coli is as simple as PCR. *PloS one* **12**, e0183974 (2017). https://doi.org/10.1371/journal.pone.0183974

70 Watson, J. F. & García-Nafría, J. In vivo DNA assembly using common laboratory bacteria: A re-emerging tool to simplify molecular cloning. *The Journal of biological chemistry* **294**, 15271–15281 (2019). https://doi.org/10.1074/jbc.REV119.009109

71 Thuring, R. W., Sanders, J. P. & Borst, P. A freeze-squeeze method for recovering long DNA from agarose gels. *Analytical biochemistry* **66**, 213–220 (1975). https://doi.org/10.1016/0003-2697(75)90739-3

72 Tautz, D. & Renz, M. An optimized freeze-squeeze method for the recovery of DNA fragments from agarose gels. *Analytical biochemistry* **132**, 14–19 (1983). https://doi.org/10.1016/0003-2697(83)90419-0

1231 73 Jin, Z. *et al.* The hyperactive Sleeping Beauty transposase SB100X improves the genetic
1232 modification of T cells to express a chimeric antigen receptor. *Gene therapy* **18**, 849–856
1233 (2011). https://doi.org/10.1038/gt.2011.40
1234 74 Kowarz, E., Loscher, D. & Marschalek, R. Optimized Sleeping Beauty transposons rapidly
1235 generate stable transgenic cell lines. *Biotechnology journal* **10**, 647–653 (2015).
1236 https://doi.org/10.1002/biot.201400821
1237 75 Laemmli, U. K. Cleavage of Structural Proteins during the Assembly of the Head of
1238 Bacteriophage T4. *Nature* **227**, 680–685 (1970). https://doi.org/10.1038/227680a0
1239 76 Schindelin, J. *et al.* Fiji: an open-source platform for biological-image analysis. *Nature methods*
1240 **9**, 676–682 (2012). https://doi.org/10.1038/nmeth.2019
1241 77 Kamentsky, L. *et al.* Improved structure, function and compatibility for CellProfiler: modular
1242 high-throughput image analysis software. *Bioinformatics (Oxford, England)* **27**, 1179–1180
1243 (2011). https://doi.org/10.1093/bioinformatics/btr095
1244 78 McQuin, C. *et al.* CellProfiler 3.0: Next-generation image processing for biology. *PLoS biology*
1245 **16**, e2005970 (2018). https://doi.org/10.1371/journal.pbio.2005970
1246 79 Stirling, D. R., Carpenter, A. E. & Cimini, B. A. CellProfiler Analyst 3.0: accessible data
1247 exploration and machine learning for image analysis. *Bioinformatics (Oxford, England)* **37**,
1248 3992–3994 (2021). https://doi.org/10.1093/bioinformatics/btab634
1249 80 Kulak, N. A., Pichler, G., Paron, I., Nagaraj, N. & Mann, M. Minimal, encapsulated proteomic-
1250 sample processing applied to copy-number estimation in eukaryotic cells. *Nature methods* **11**,
1251 319–324 (2014). https://doi.org/10.1038/nmeth.2834
1252 81 Tyanova, S., Temu, T. & Cox, J. The MaxQuant computational platform for mass spectrometry-
1253 based shotgun proteomics. *Nature protocols* **11**, 2301–2319 (2016).
1254 https://doi.org/10.1038/nprot.2016.136
1255 82 Olivella, R. *et al.* QCloud2: An Improved Cloud-based Quality-Control System for Mass-
1256 Spectrometry-based Proteomics Laboratories. *Journal of proteome research* **20**, 2010–2013
1257 (2021). https://doi.org/10.1021/acs.jproteome.0c00853
1258 83 Wieczorek, S. *et al.* DAPAR & ProStaR: software to perform statistical analyses in quantitative
1259 discovery proteomics. *Bioinformatics (Oxford, England)* **33**, 135–136 (2017).
1260 https://doi.org/10.1093/bioinformatics/btw580
1261 84 Pounds, S. & Cheng, C. Robust estimation of the false discovery rate. *Bioinformatics (Oxford,*
1262 *England)* **22**, 1979–1987 (2006). https://doi.org/10.1093/bioinformatics/btl328
1263 85 Smyth, G. K. Linear models and empirical bayes methods for assessing differential expression
1264 in microarray experiments. *Statistical applications in genetics and molecular biology* **3**,
1265 Article3 (2004). https://doi.org/10.2202/1544-6115.1027
1266 86 Giai Gianetto, Q. *et al.* Calibration plot for proteomics: A graphical tool to visually check the
1267 assumptions underlying FDR control in quantitative experiments. *Proteomics* **16**, 29–32
1268 (2016). https://doi.org/10.1002/pmic.201500189

1269

NF-kB p65 interactome is divergent between TIGR and 6B ST90

FIG 1

A

p65 mass spectrometry interactome (4x biological)

B

Summary of unique proteins to uninfected GFP - control	
6B ST90 up	709 proteins
6B ST90 down	403 proteins
TIGR4 up	1120 proteins
TIGR4 down	874 proteins

C

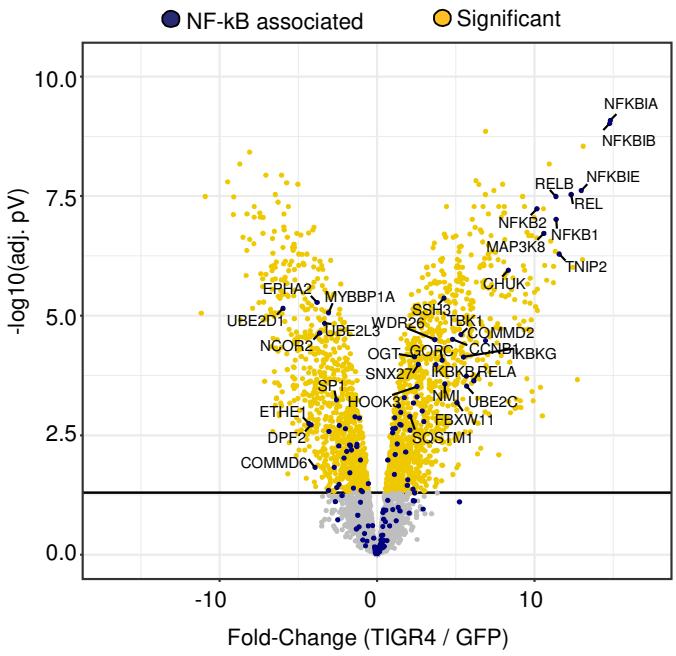

D

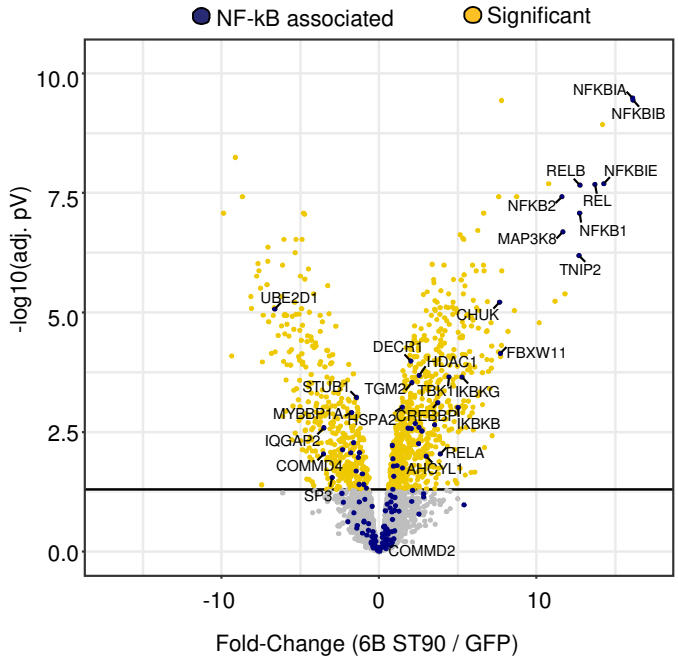

E

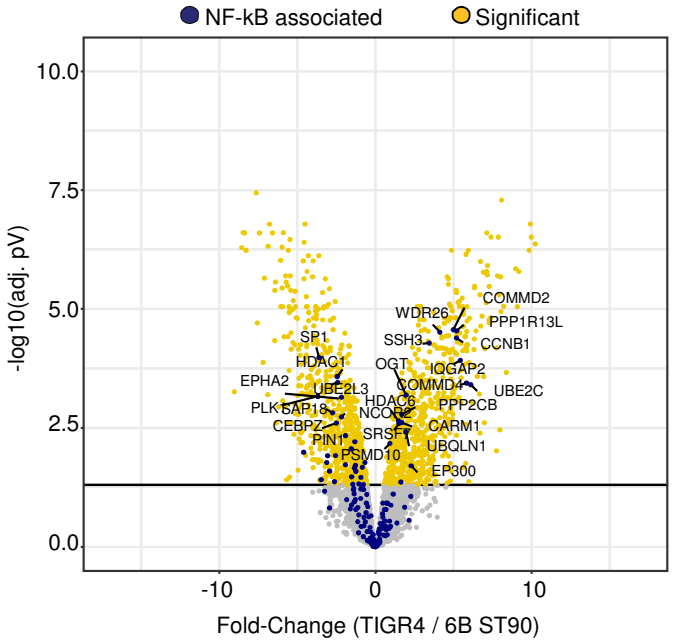

F

TIGR4 vs. 6B ST90 positive enrichment

STRING GO Ontology (Biological Process)			
#term ID	**Term Description**	**strength**	**FDR**
GO:1905337	Positive regulation of aggrephagy	1.63	0.0162
GO:1905821	Positive regulation of chromosome condensation	1.41	0.0341
GO:0007091	Metaphase/anaphase transition of mitotic cell cycle	1.33	0.0097
GO:1902966	Positive regulation of protein localization to early endosome	1.33	0.0097
GO:2000643	Positive regulation of early endosome to late endosome transport	1.33	0.0097
GO:0090522	Vesicle tethering involved in exocytosis	1.28	0.0123
GO:0033147	Negative regulation of intracellular estrogen receptor signaling pathway	1.24	0.00081
GO:0048194	Golgi vesicle budding	1.24	0.0162
GO:0010968	Regulation of microtubule nucleation	1.19	0.02
GO:0051469	Vesicle fusion with vacuole	1.19	0.02

Individual in NF-kB p65 show differential enrichment of partners and biological processes

Sup. FIG 1

A

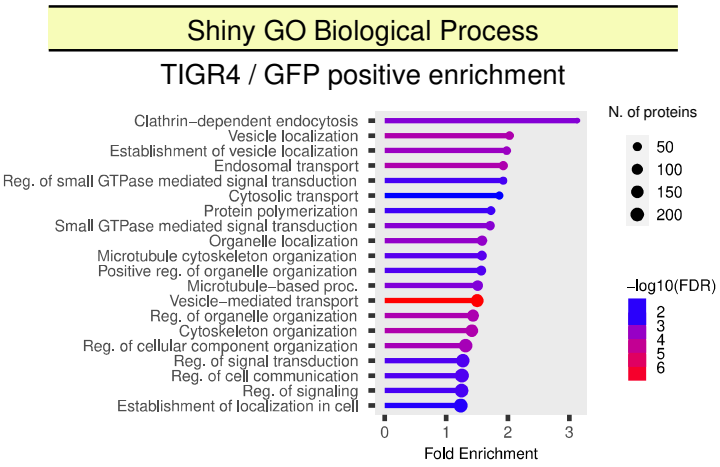

B

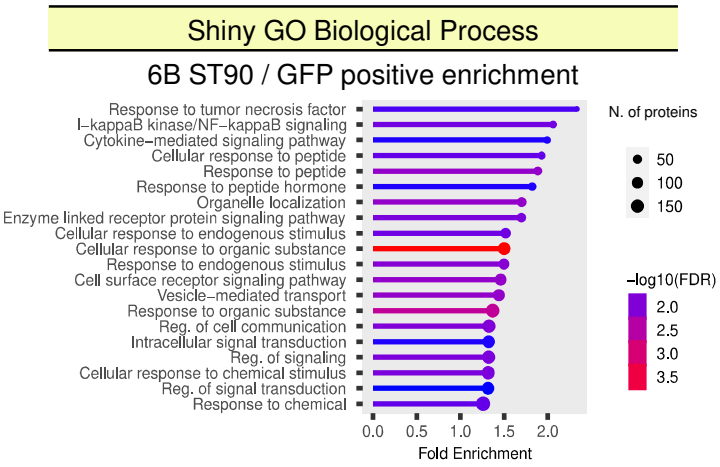

TIGR4 differentially engages NF-kB p65 in comparison to commensal-like 6B ST90

FIG 2

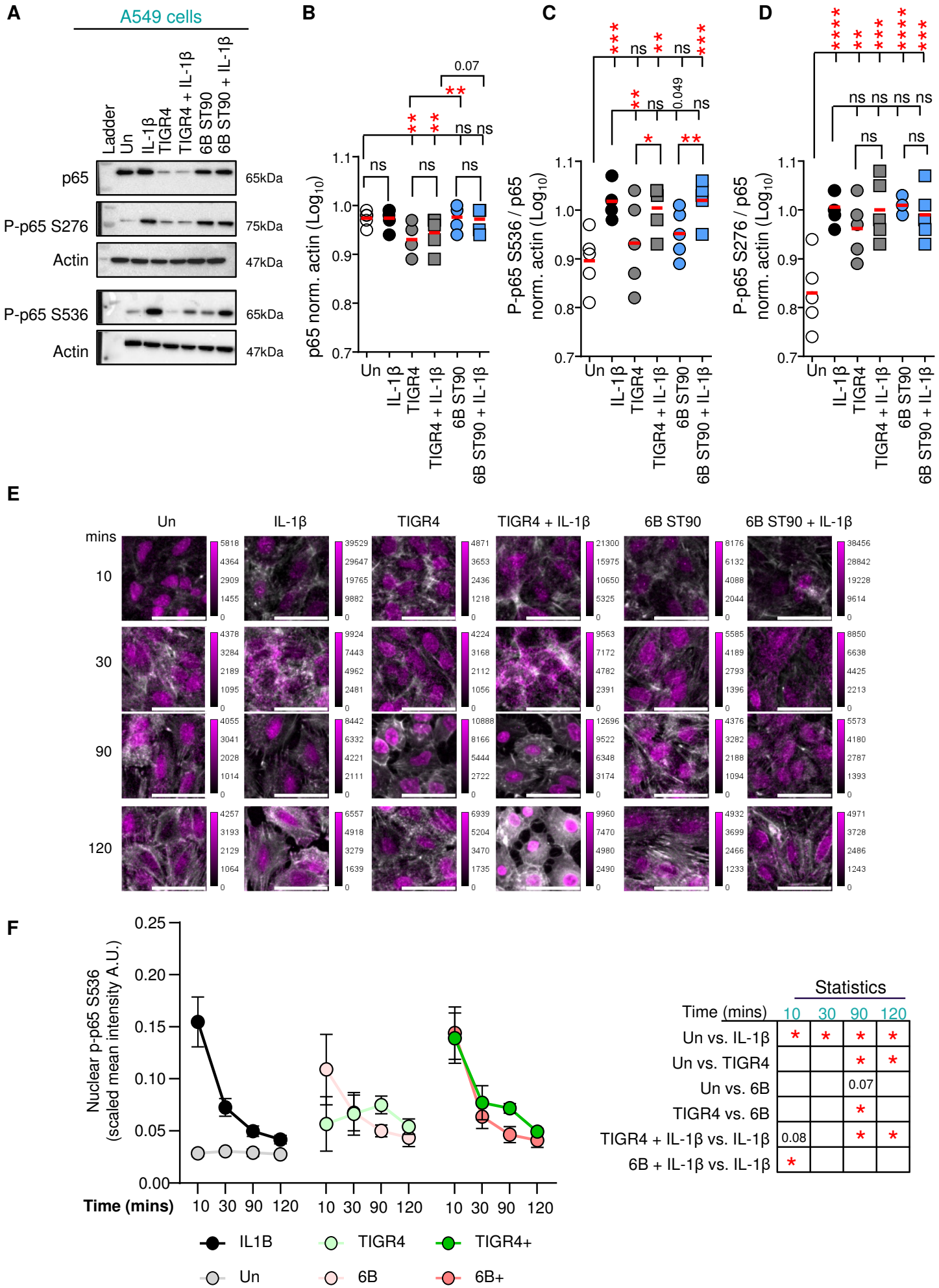

TIGR4 drives disparity in NF-kB p65 driven gene expression and chromatin binding

Sup. FIG 2

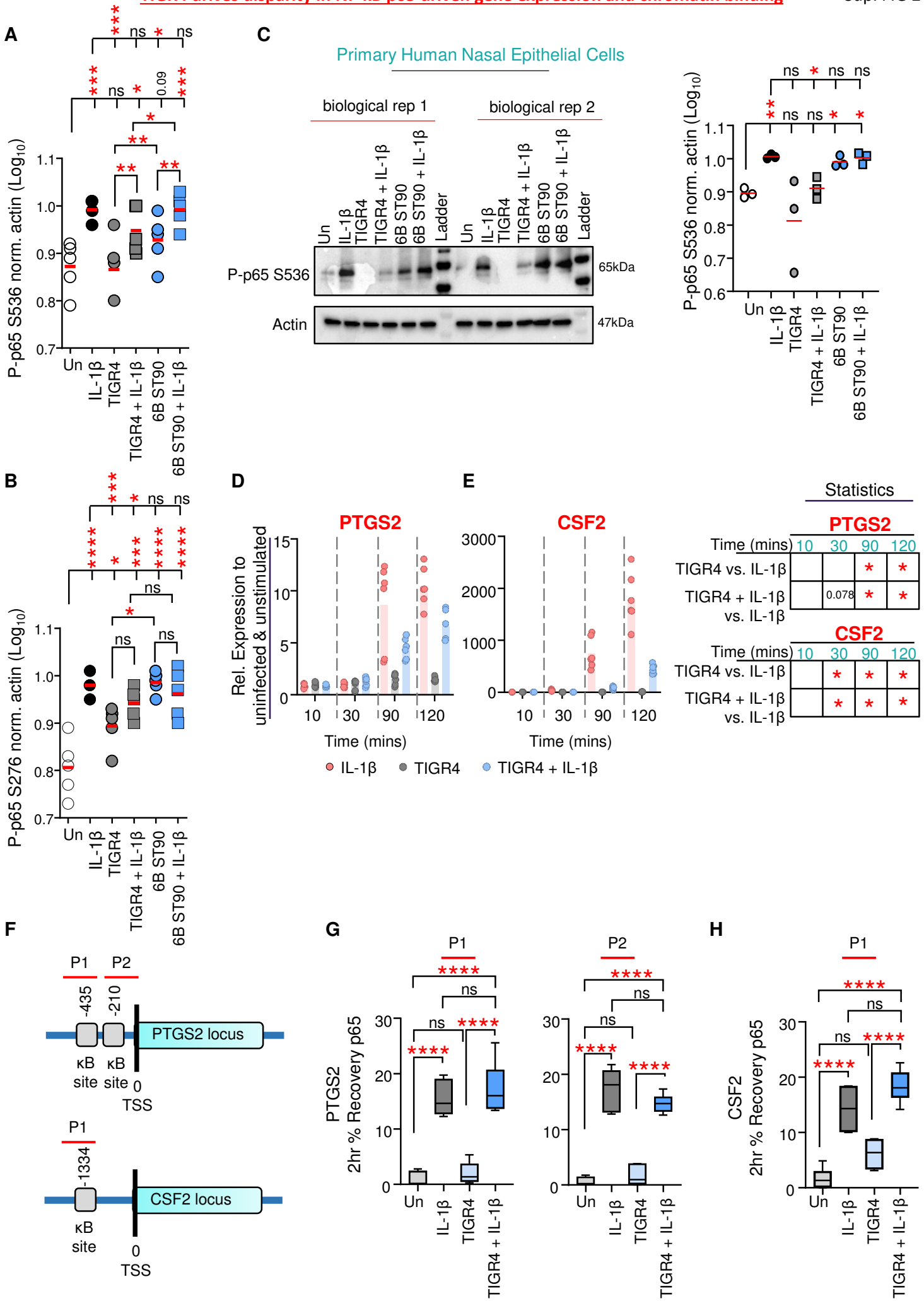

Blocking autophagy increases total COMMD2 and NF-kB p65 during TIGR4 challenge

FIG 3

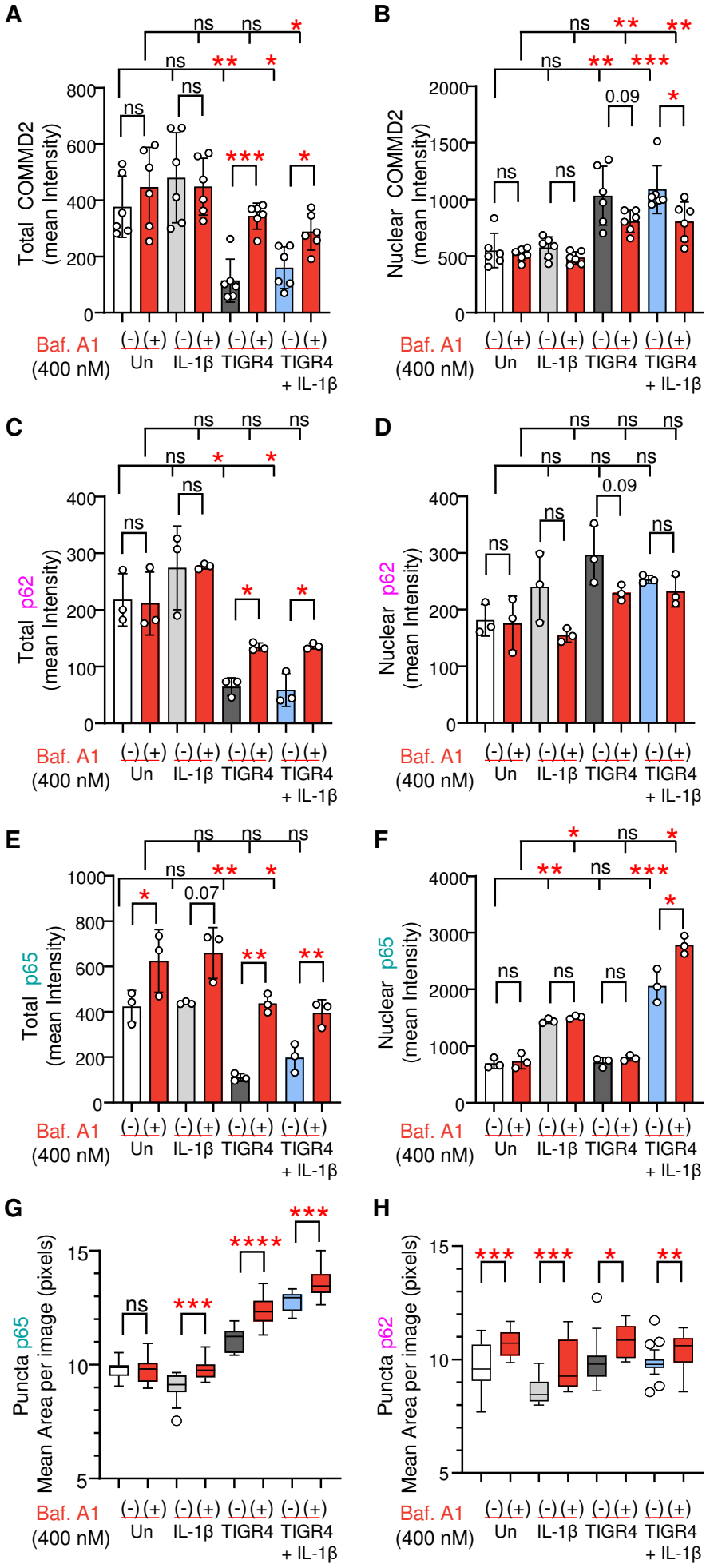

Representative images of COMMD2 and NF-kB p65

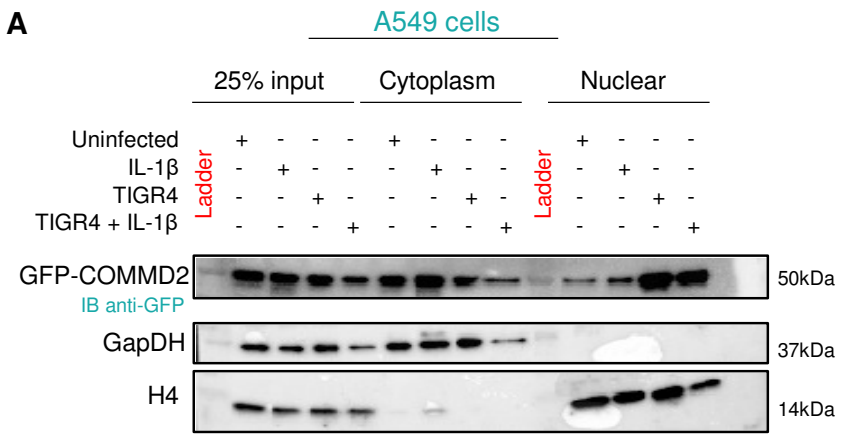

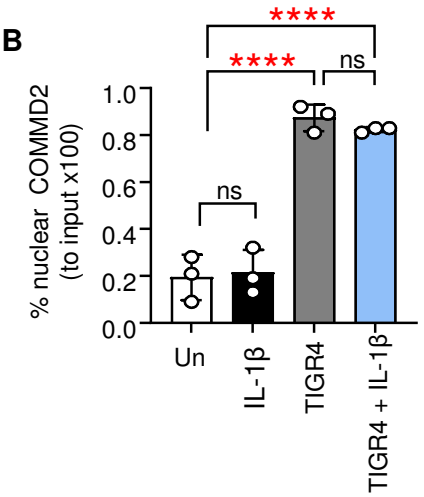

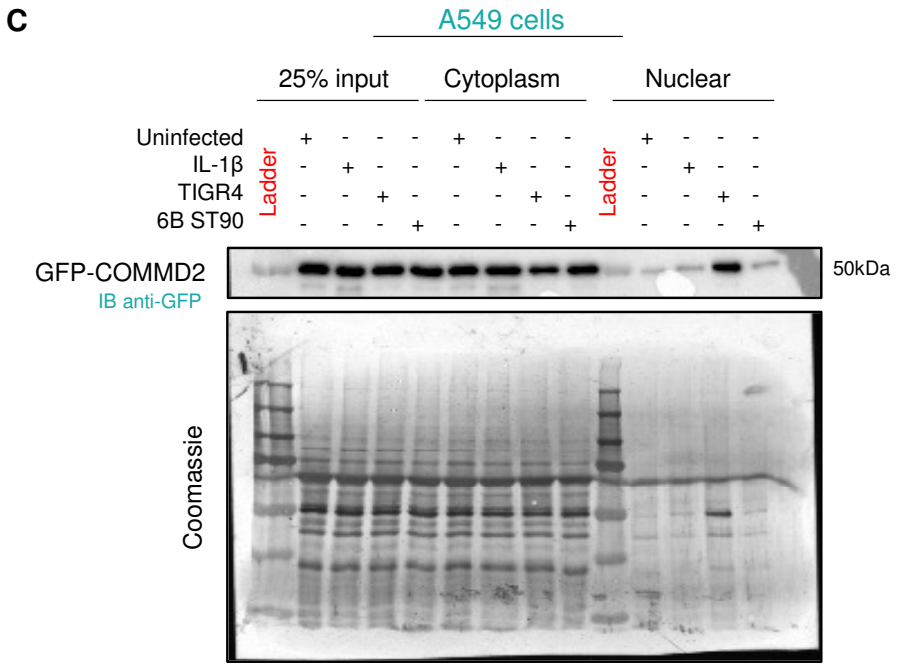

Representative images of COMMD2 and NF-kB p65

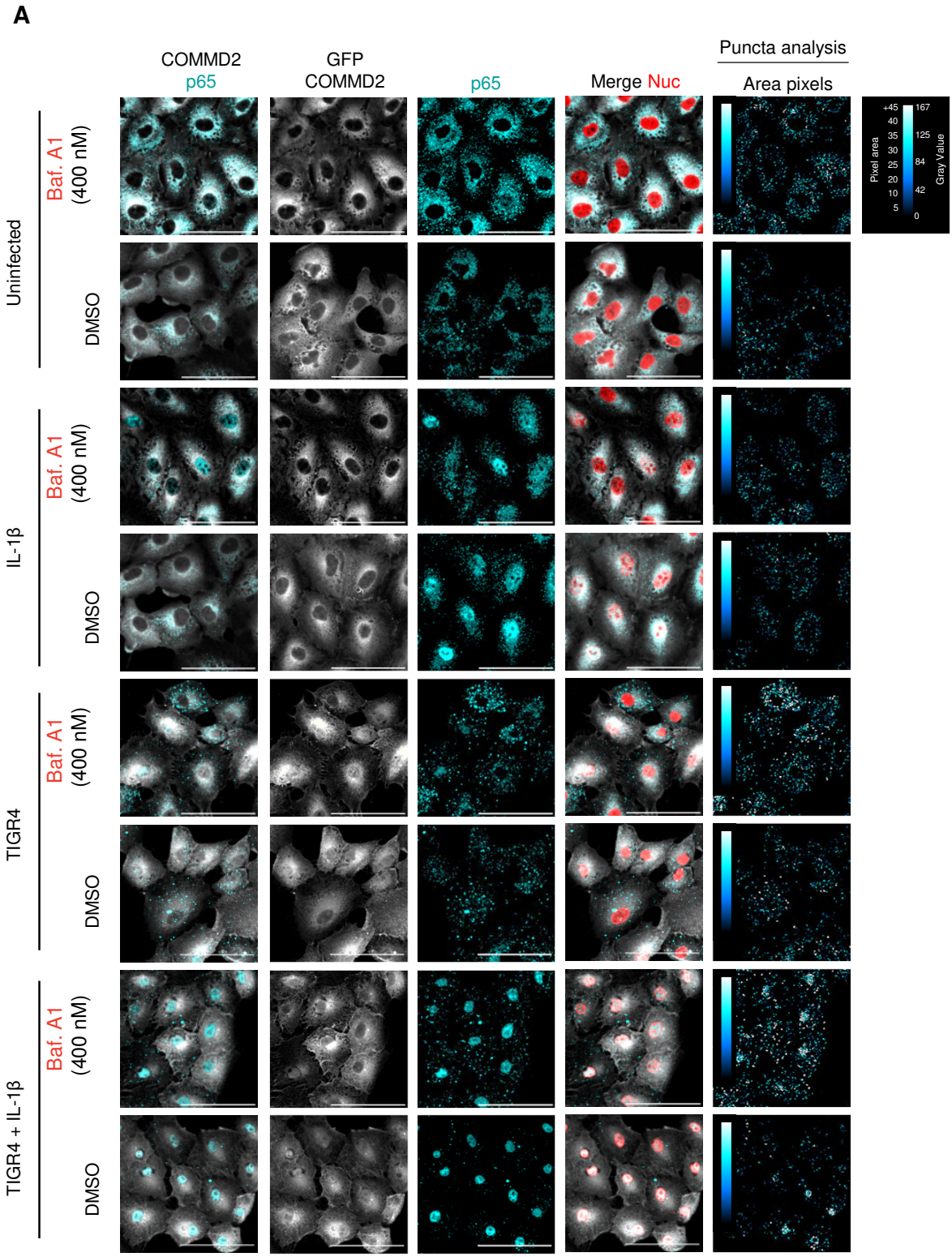

A

Representative images of COMMD2 and p62

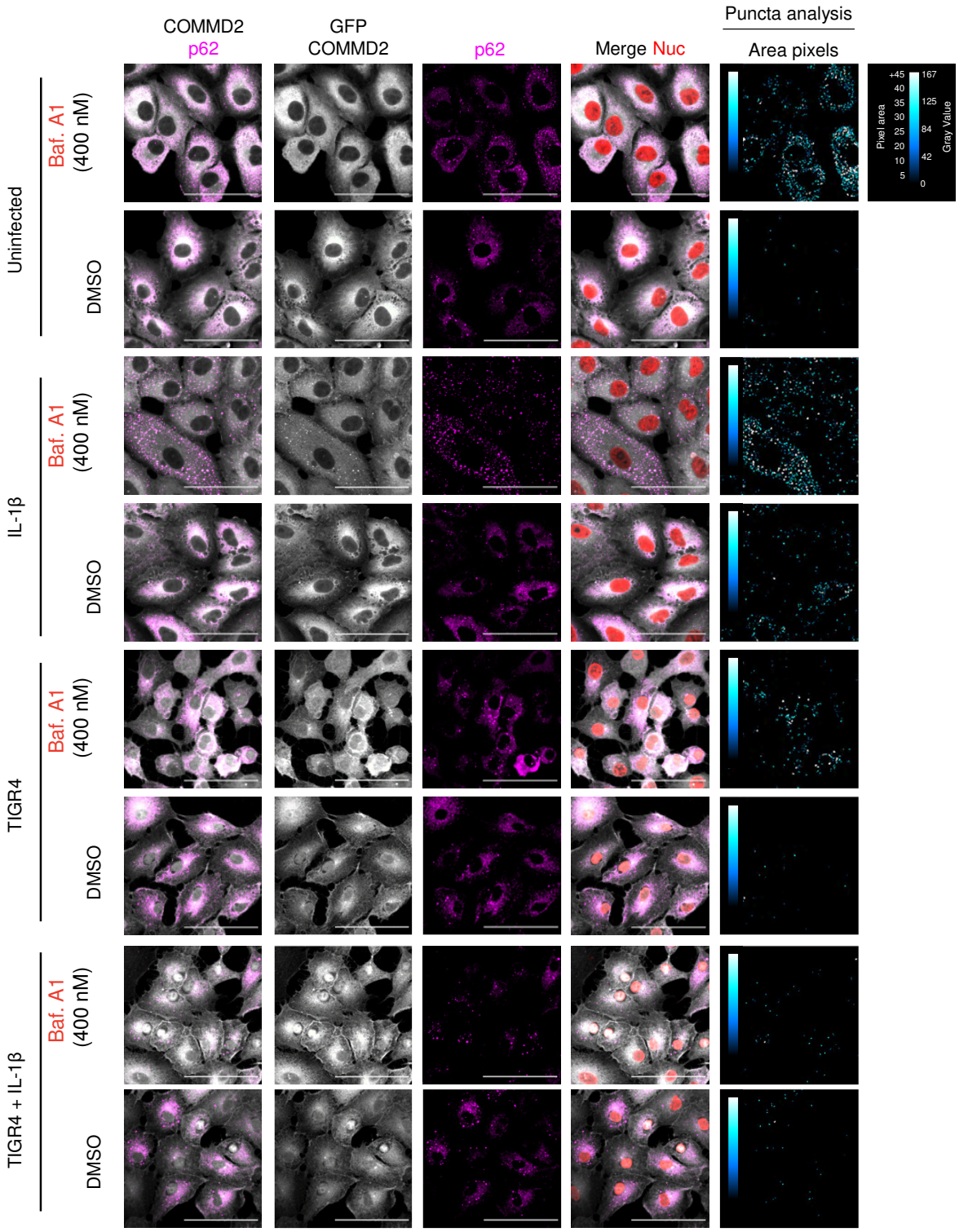

TIGR4 drives NF-kB p65 interaction with COMMD2 and p62 (SQSTM1)

FIG 4

A549 GFP-COMMD2 cells

A

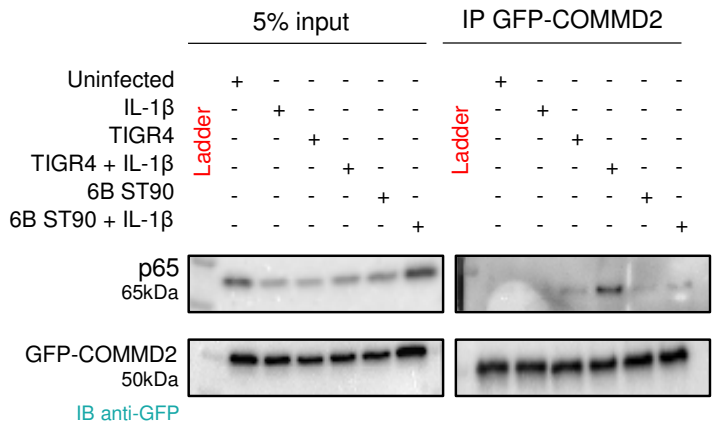

B

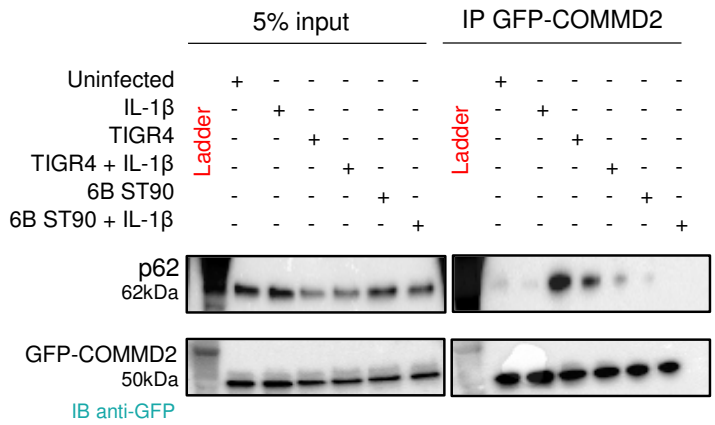

TIGR4 induces an endogenous complex of NF-kB p65 – COMMD2

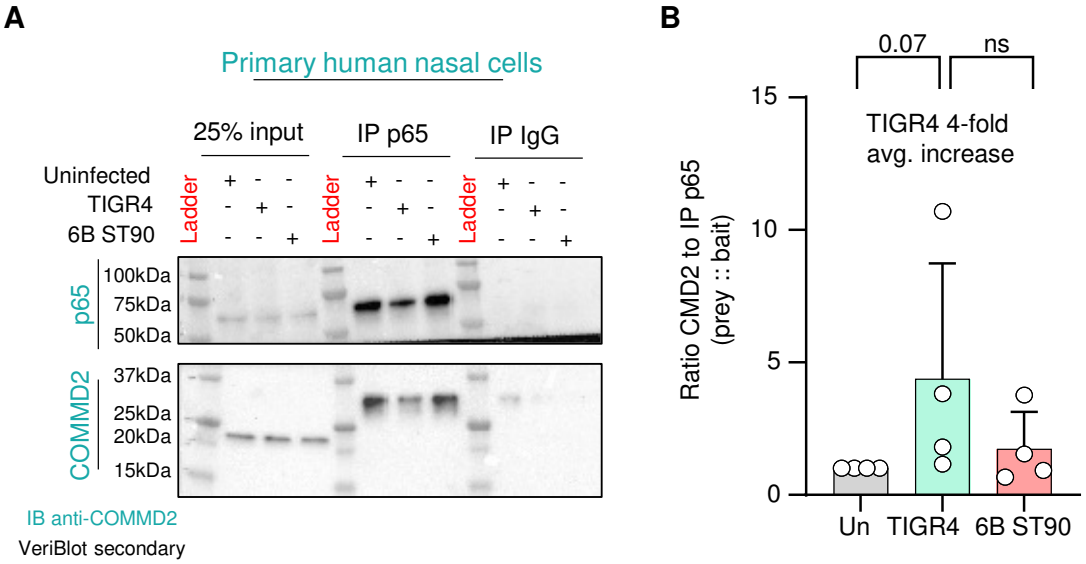

COMMD2-p65-p62 is exported from nucleus through CRM1

FIG 5

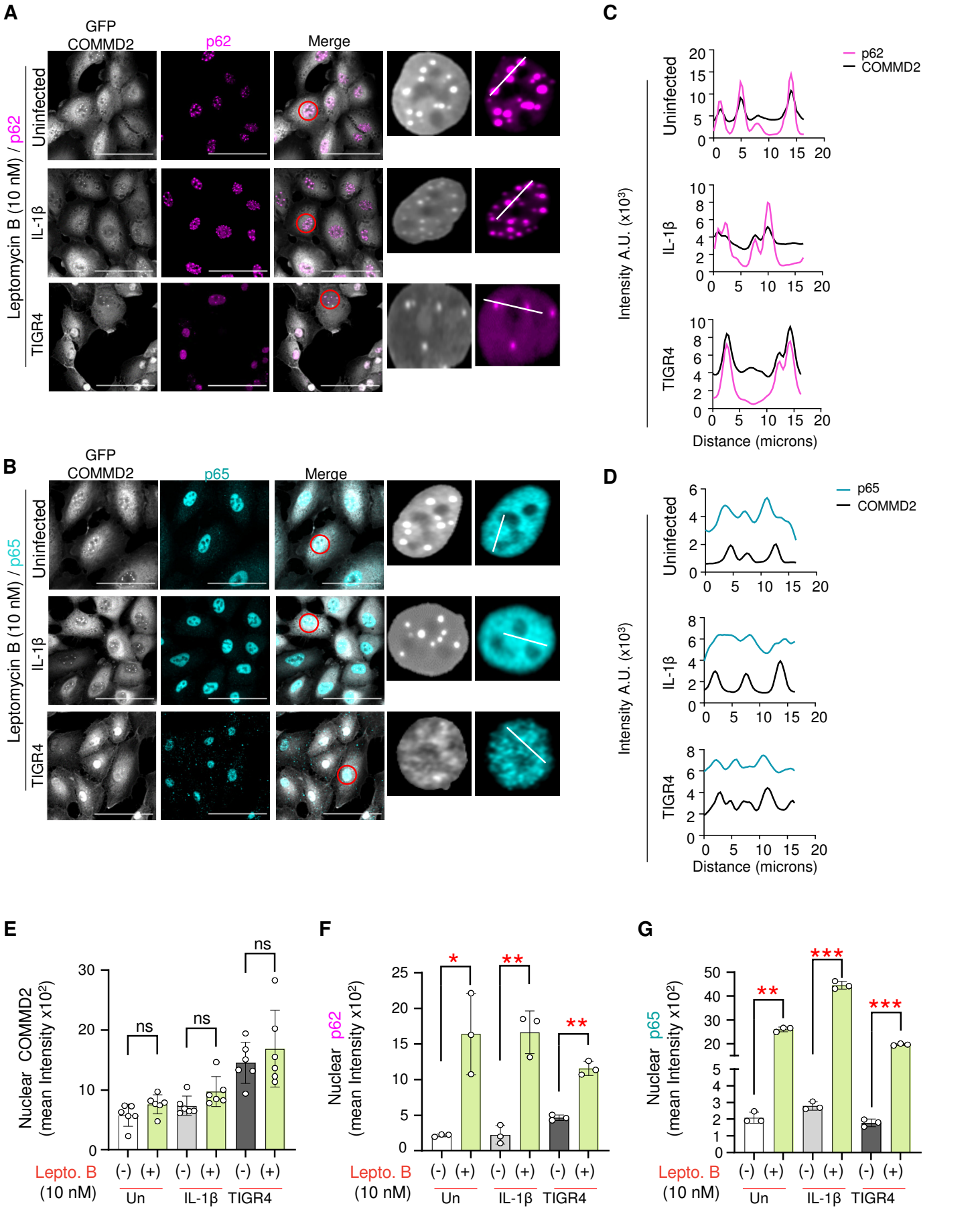

Inhibition of CRM1 increases p62 puncta when cells are challenged with TIGR4 + IL-1β

Sup. FIG 7

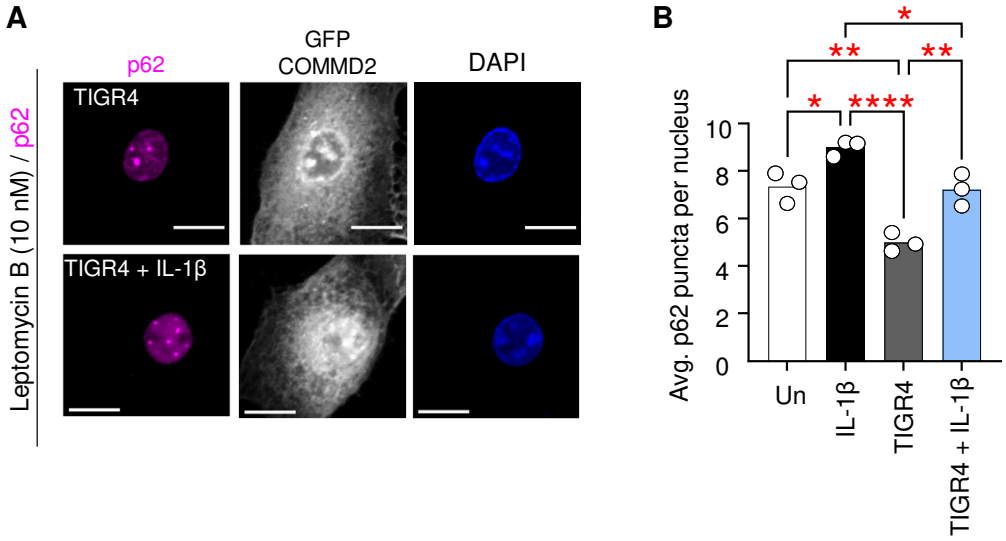

TIGR4 induces a unique COMMD2 interactome, enriched with NF-kB associated partners

FIG 6

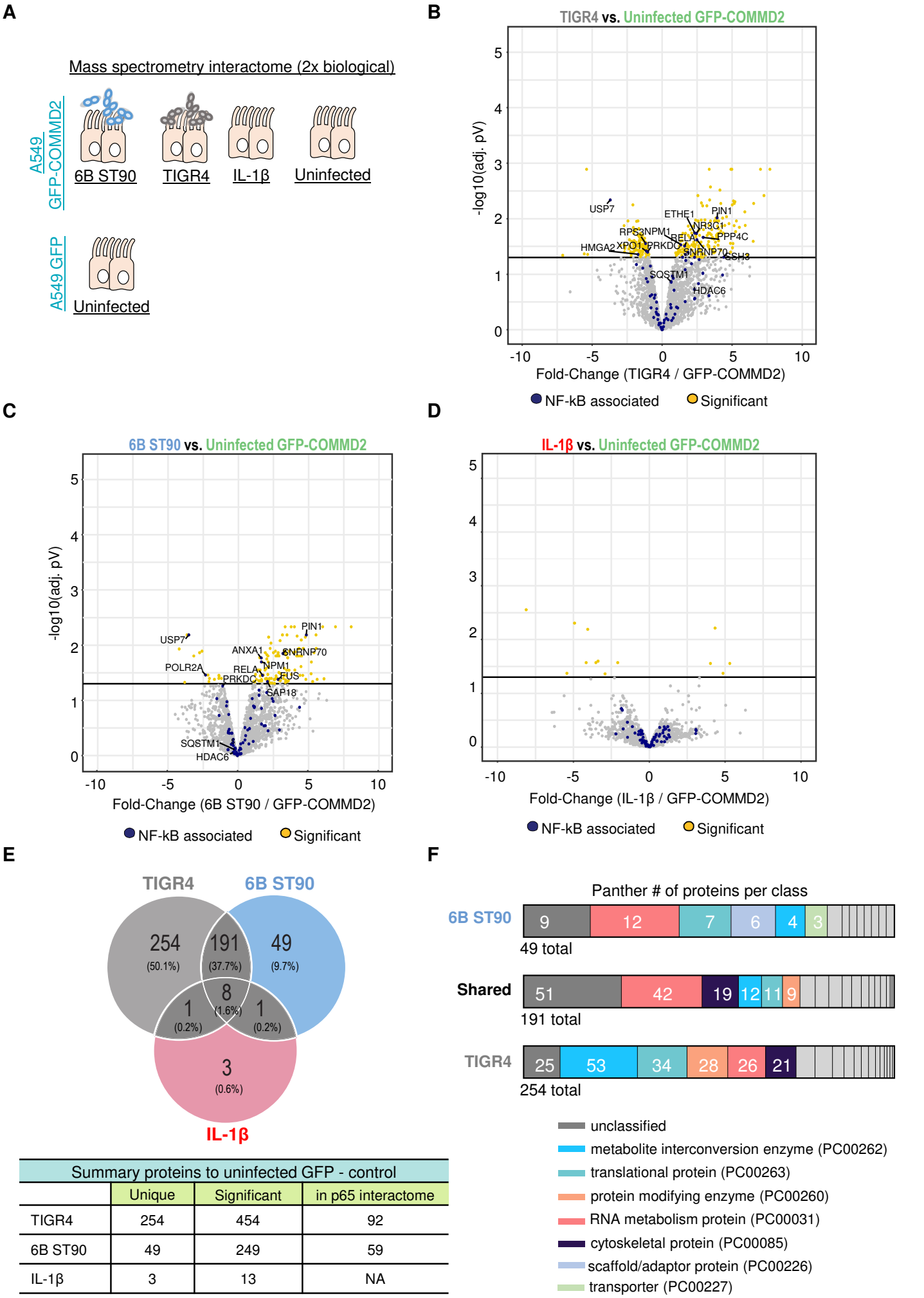

Summary proteins to uninfected GFP - control			
	Unique	Significant	in p65 interactome
TIGR4	254	454	92
6B ST90	49	249	59
IL-1β	3	13	NA

A

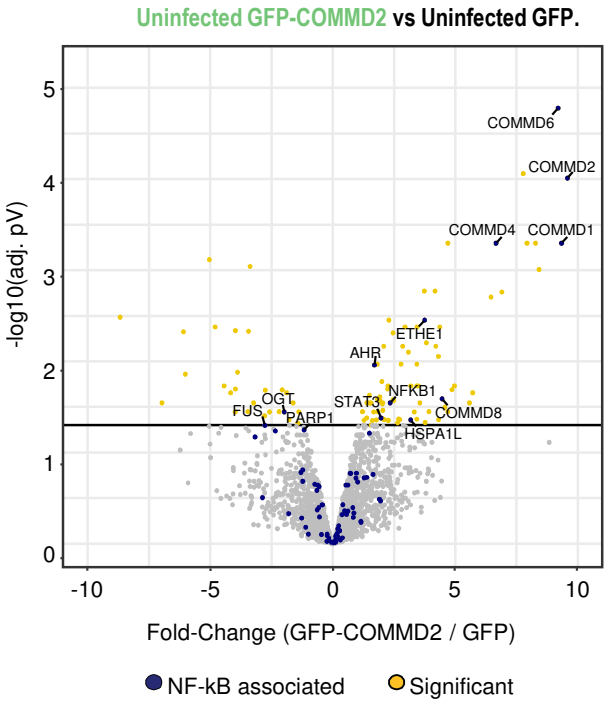
Uninfected GFP-COMMD2 vs Uninfected GFP.
-log10(adj. pV)
Fold-Change (GFP-COMMD2 / GFP)
COMMD6
COMMD2
COMMD4
COMMD1
ETHE1
AHR
NFKB1
STAT3
COMMD8
HSPA1L
OGT
FUS
PARP1
NF-kB associated
Significant

COMMD2 RNAi selectively elevates secreted cellular immunity landscape

FIG 7

A

Primary human nasal cells

	RNAi COMMD2						Significance to Scr					
	Un.	IL-1β	TIGR4	6B ST90	TIGR4 + IL-1β	6B ST90 + IL-1β	Un.	IL-1β	TIGR4	6B ST90	TIGR4 + IL-1β	6B ST90 + IL-1β
CCL3	0.153	0.003	0.477	1.243	0.117	0.007	0.3740	0.9700	0.3440	0.3998	0.2950	0.9620
CCL20	0.243	0.460	0.693	0.707	0.700	0.467	0.1560	0.4040	0.1170	0.0273	0.0130	0.0050
CXCL1	0.443	0.287	0.433	0.253	-0.047	0.070	0.0200	0.2530	0.0250	0.2251	0.8340	0.5230
CXCL10	1.927	1.400	1.690	1.863	1.553	0.940	0.0580	0.0110	0.0400	0.0150	0.0410	0.0460
ICAM1	-1.120	-0.620	1.197	-1.033	0.010	1.227	0.3740	0.3650	0.4800	0.1194	0.9740	0.3780
IL1ra (IL1RN)	0.267	-0.160	0.377	0.407	0.200	0.343	0.4710	0.3440	0.1510	0.0094	0.0020	0.0550
IL-8	0.740	0.217	0.570	0.187	0.057	-0.453	0.0270	0.6320	0.1970	0.6087	0.8880	0.3560
IL11	1.237	0.287	1.600	0.963	0.157	0.307	0.0630	0.1120	0.2260	0.3411	0.4190	0.1620
IL-13	-0.070	0.257	0.100	0.547	-0.150	0.330	0.9360	0.6070	0.8600	0.4551	0.3740	0.5280
IL-18	-1.137	1.467	-0.080	0.097	-0.187	0.153	0.5300	0.3550	0.8510	0.8067	0.5310	0.1420
MMP2	1.910	0.123	0.463	0.023	0.070	0.107	0.4370	0.1230	0.2520	0.9012	0.6890	0.3740
MMP9	-0.007	0.097	-0.080	-0.050	-0.133	-0.057	0.3740	0.9140	0.9280	0.8559	0.8170	0.8960
SELE	0.033	0.377	-0.250	-0.077	0.383	0.353	0.3740	0.4230	0.3740	0.3739	0.4840	0.1470
SLPI	0.140	0.323	0.277	0.263	0.277	0.200	0.3370	0.1710	0.0630	0.1381	0.0640	0.2820
SCGB1A	0.170	0.153	0.117	0.090	-0.187	-0.067	0.3590	0.3110	0.4310	0.2566	0.5460	0.5030
CX3CL1	0.887	-0.050	0.247	1.063	1.013	1.130	0.1170	0.8340	0.5760	0.3729	0.3650	0.3630
CXCL2	0.337	-0.017	0.160	0.170	-0.080	-0.163	0.2870	0.8760	0.3470	0.4595	0.7970	0.5700
CSF2	0.147	-0.070	-0.100	0.177	-0.140	-0.100	0.3740	0.5280	0.8380	0.7149	0.5930	0.1440
IFNA1	-0.107	-0.167	-0.157	0.217	0.007	-0.017	0.3740	0.3740	0.3740	0.5104	0.9610	0.9040
IL-6	-0.083	-0.260	-0.130	-0.157	-0.143	-0.090	0.8360	0.1260	0.5530	0.5429	0.5320	0.7040
IL-10	0	0.437	-0.643	0.463	0.330	0.657		0.3230	0.3740	0.3739	0.1410	0.2740
IL-17C	0.393	-0.637	-0.040	-0.153	-1.763	-1.423	0.3740	0.2740	0.9830	0.3739	0.2480	0.1130
MMP1	0.020	-0.170	0.463	0.057	0.033	0.050	0.8440	0.4830	0.1940	0.6977	0.9160	0.7460
MMP3	0.750	0.037	0.087	0.027	0.357	-0.337	0.2340	0.8800	0.8420	0.9159	0.3430	0.0970
PTX3	0.243	0.277	-0.343	1.143	0.717	0.997	0.3740	0.1370	0.7060	0.0263	0.0840	0.1290
SELP	1.297	-0.030	0.060	-0.027	0.127	0.480	0.1420	0.8140	0.8400	0.6087	0.3240	0.4240
TNFa	0	-0.837	1.217	-0.093	-0.613	-0.523		0.1840	0.3770	0.1181	0.2420	0.1390

Not calculated | Borderline | pV ≤0.05

-1 0 1

4hr Avg. Luminex Analyte Expression to individual Scr control (log_2)

B

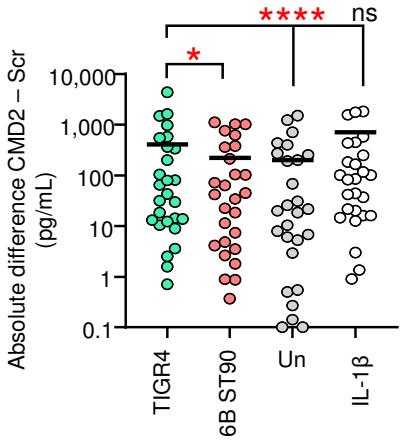

C

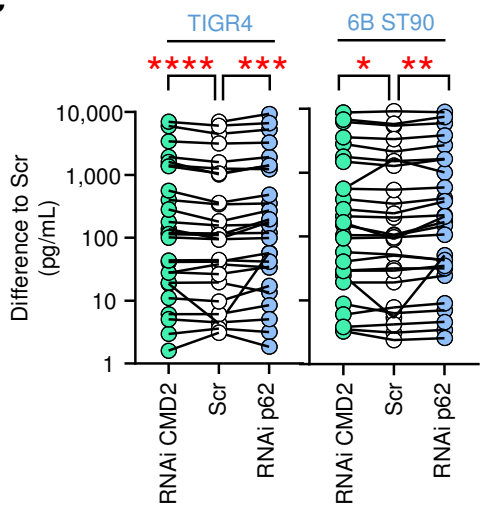

D

NF-kB motif prediction

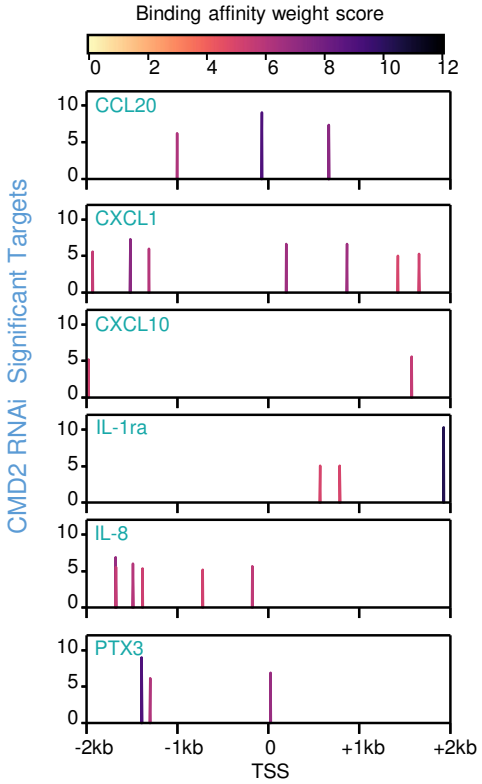

E

NF-kB motif predicted sequence alignment

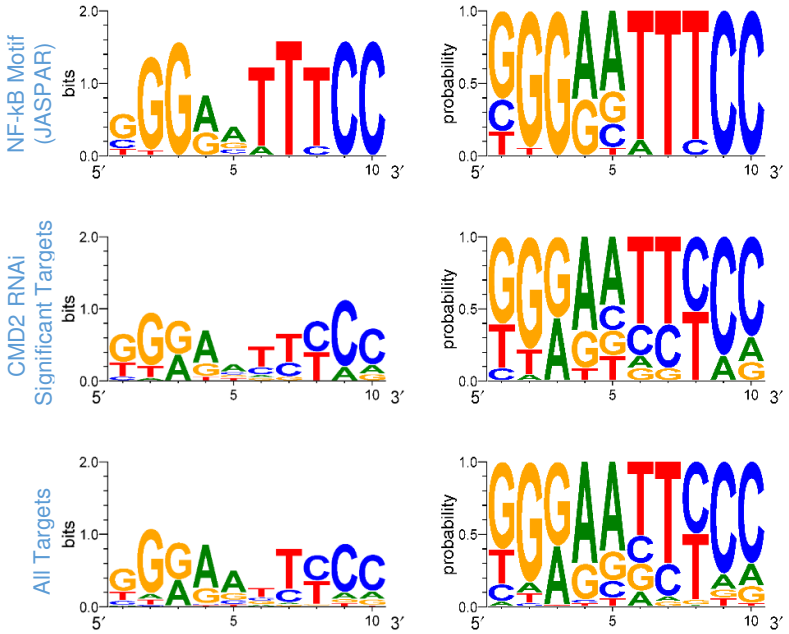

COMMD2 RNAi is effective in primary nasal cells

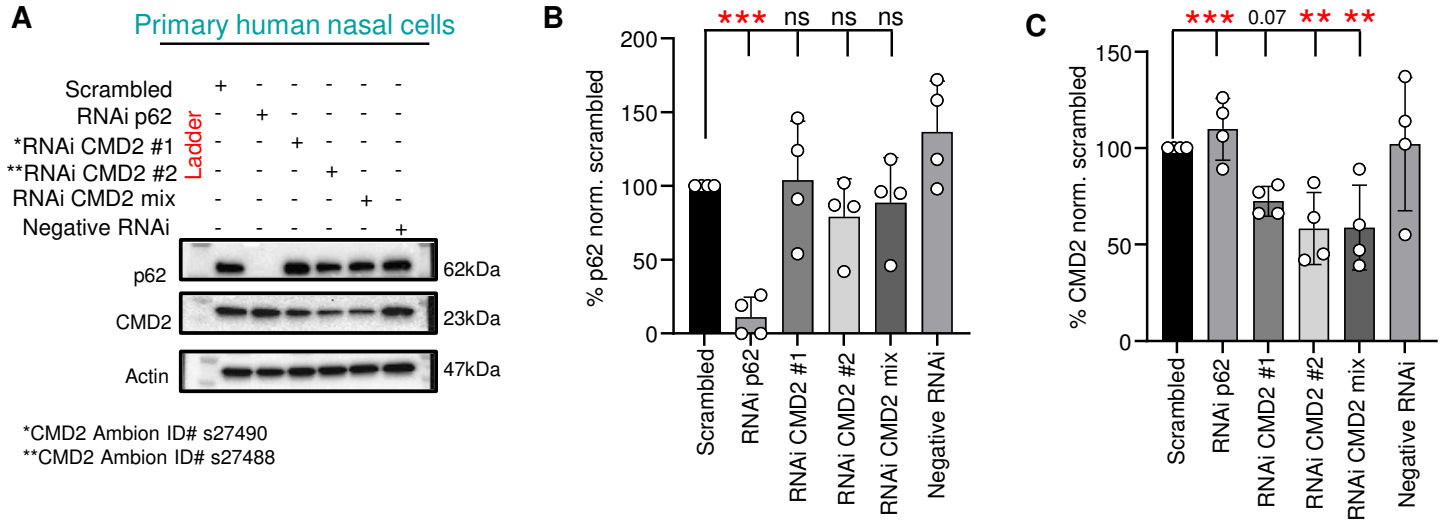

Primary human nasal cells

D

To Scr uninfected

	IL-1β	TIGR4	6B ST90	TIGR4 + IL-1β	6B ST90 + IL-1β
CCL3	1.977	1.343	0.473	1.917	2.063
CCL20	2.863	1.023	1.133	2.743	2.770
CXCL1	1.600	0.427	0.580	1.893	1.890
CXCL10	3.113	0.950	1.263	2.793	3.123
ICAM1	3.680	1.527	1.967	2.510	2.490
IL1ra (IL1RN)	0.357	1.270	1.703	1.480	1.763
IL-8	2.723	1.460	1.543	3.090	3.390
IL11	3.287	0.990	1.657	3.473	3.493
IL-13	0.867	0.440	0	1.490	1.157
IL-18	1.023	0.347	0.300	1.317	0.913
MMP2	4.107	2.763	3.140	4.217	4.243
MMP9	0.663	0.400	0.393	0.893	1.103
SELE	1.100	0.677	0.503	1.280	1.313
SLPI	0.333	0.273	0.197	0.427	0.310
SCGB1A	0.307	0.520	0.553	0.740	0.683
CX3CL1	1.810	1.310	1.473	1.930	1.863
CXCL2	4.113	1.577	1.547	4.653	4.613
CSF2	2.220	0.533	0.507	2.510	2.440
IFNA1	0.433	0.313	0.070	0.467	0.470
IL-6	5.320	1.940	1.797	6.157	5.943
IL-10	0.923	0.643	0.397	1.083	1.387
IL-17C	4.763	0.910	0.097	4.850	6.480
MMP1	0.890	0.477	0.647	0.920	0.807
MMP3	2.147	1.400	1.463	2.233	2.397
PTX3	2.030	0.863	0.340	2.280	2.240
SELP	2.917	2.397	2.383	3.217	2.973
TNFa	5.110	0.447	1.450	6.007	5.580

0 2 4 6

4hr Avg. Luminex Analyte Expression to uninfected Scr control (log_2)

E

RNAi p62

	Un.	IL-1β	TIGR4	6B ST90	TIGR4 + IL-1β	6B ST90 + IL-1β
CCL3	0.260	-0.037	0.040	1.210	0.143	-0.017
CCL20	0.073	0.137	0.700	0.620	0.657	0.200
CXCL1	0.137	0.113	0.173	0.087	-0.130	-0.200
CXCL10	3.423	2.447	3.347	3.067	2.777	2.357
ICAM1	0.933	-0.790	0.237	0.287	1.100	0.757
IL1ra (IL1RN)	0.153	0.200	0.357	0.437	0.503	0.513
IL-8	0.587	0.250	0.370	0.163	0.283	-0.283
IL11	0.483	0.103	1.040	0.687	0.093	0.033
IL-13	0.660	0.037	0.113	0.973	0	0.087
IL-18	0.077	0.023	0.320	-0.177	-0.223	0.967
MMP2	1.460	0.083	0.273	0.100	0.010	-0.070
MMP9	0	0.403	-0.400	0.303	0.237	-0.263
SELE	0.033	0.017	-0.090	0	0.413	0.120
SLPI	0.093	0.200	0.090	0.303	0.300	0.320
SCGB1A	0.207	0.280	0.063	0.217	0.127	0.100
CX3CL1	1.267	0.100	0.263	0.200	-0.013	0.020
CXCL2	0.087	-0.130	-0.013	0.130	-0.163	-0.130
CSF2	0.120	-0.077	0.380	0.093	-0.063	0.083
IFNA1	0.017	-0.067	-0.100	0.180	-0.033	-0.260
IL-6	0.077	-0.467	-0.147	-0.290	-0.450	-0.553
IL-10	0	0.710	-0.483	0.063	0.613	0.323
IL-17C	1.477	-1.073	-0.367	0.080	2.320	-0.737
MMP1	0.340	0.257	0.447	0.570	0.493	0.497
MMP3	0.600	-0.083	0.303	0.200	0.023	-0.307
PTX3	0.263	0.693	0.427	0.950	0.317	0.453
SELP	1.747	0.190	0.040	0.087	0.187	-0.070
TNFa	0.387	-0.527	1.200	0.080	-0.453	-0.263

-1 0 1 2 3

4hr Avg. Luminex Analyte Expression to individual Scr control (log_2)

Significance to Scr

	Un.	IL-1β	TIGR4	6B ST90	TIGR4 + IL-1β	6B ST90 + IL-1β
CCL3	0.1420	0.7760	0.6940	0.3637	0.3870	0.8420
CCL20	0.8780	0.6810	0.1160	0.0044	0.0070	0.3800
CXCL1	0.5980	0.5560	0.2270	0.4627	0.4890	0.0380
CXCL10	0.0060	0.0010	0.0020	0.0004	0.0020	0.0020
ICAM1	0.3740	0.2410	0.8040	0.8613	0.3910	0.5940
IL1ra (IL1RN)	0.7580	0.3880	0.1360	0.1112	0.0360	0.0620
IL-8	0.0470	0.6170	0.2370	0.6062	0.5020	0.1870
IL11	0.1410	0.5380	0.1800	0.3629	0.6230	0.7520
IL-13	0.3740	0.9630	0.7140	0.1902	1.0000	0.8100
IL-18	0.8740	0.9550	0.1300	0.6342	0.5400	0.5020
MMP2	0.4550	0.3210	0.5470	0.1755	0.9340	0.1170
MMP9		0.5440	0.3740	0.1298	0.2030	0.3740
SELE	0.3740	0.9500	0.3740		0.3520	0.4250
SLPI	0.5310	0.2440	0.3880	0.0226	0.0920	0.0930
SCGB1A	0.4320	0.2200	0.4350	0.2467	0.4610	0.5550
CX3CL1	0.1210	0.4880	0.5900	0.3068	0.9280	0.8180
CXCL2	0.8540	0.3120	0.9200	0.4146	0.1670	0.0230
CSF2	0.1190	0.8210	0.2730	0.3739	0.6730	0.6150
IFNA1	0.9350	0.7480	0.3740	0.5329	0.8480	0.1780
IL-6	0.8450	0.0070	0.3030	0.4049	0.0620	0.0400
IL-10		0.4030	0.6100	0.3739	0.2670	0.3190
IL-17C	0.1950	0.1560	0.8460	0.3739	0	0.3280
MMP1	0.0530	0.3240	0.1420	0.0003	0.1060	0.0870
MMP3	0.1980	0.7950	0.3740	0.5122	0.9000	0.1130
PTX3	0.1190	0.1420	0.5190	0.1228	0.2890	0.2140
SELP	0.1240	0.5410	0.8950	0.5686	0.6530	0.1580
TNFa	0.1380	0.0860	0.3960	0.5309	0.1140	0.0240

Not calculated | Borderline | pV ≤0.05

COMMD2 nuclear localization predominately favors invasive pneumococcal isolates with functional PLY

FIG 8

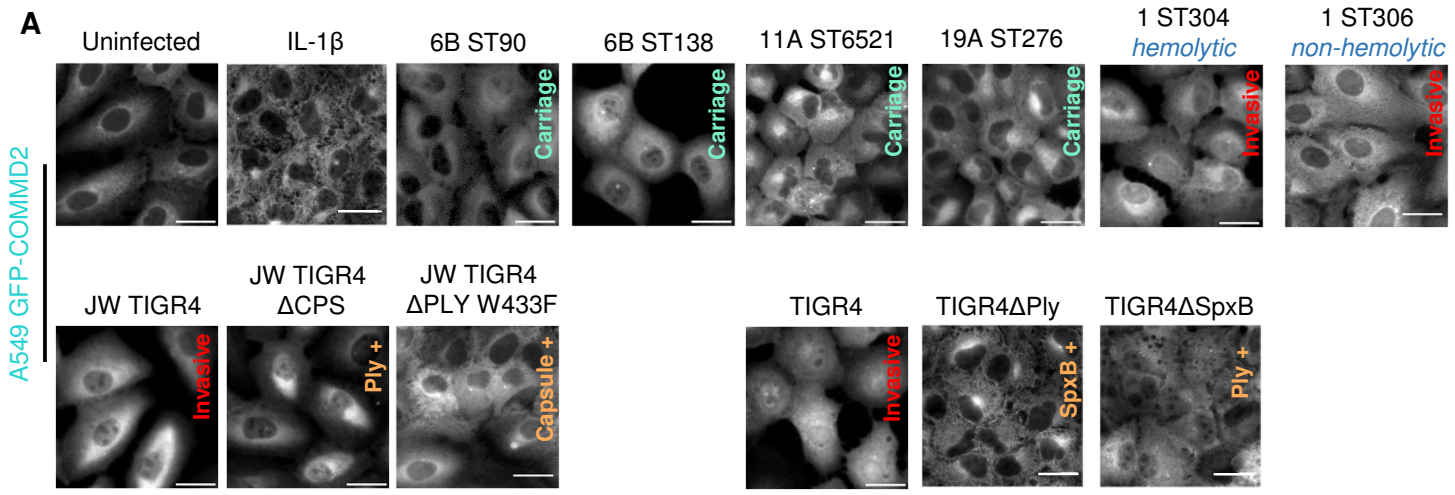

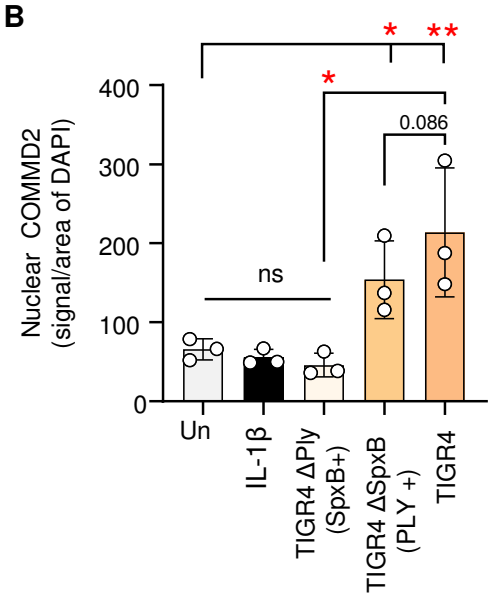

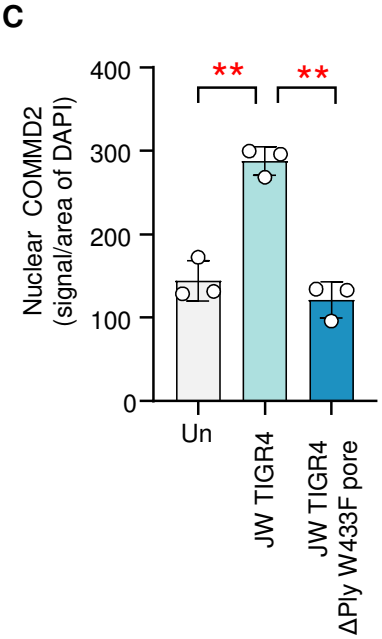

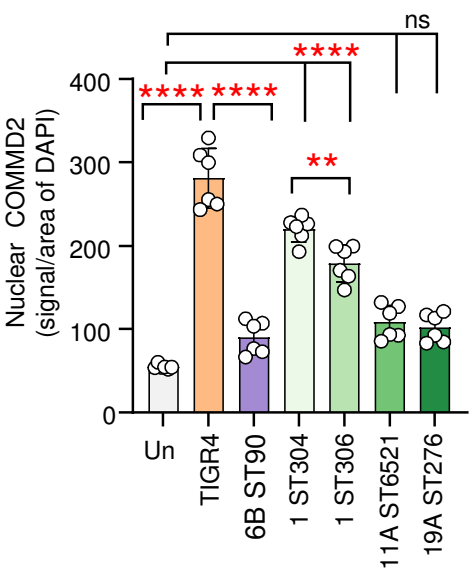

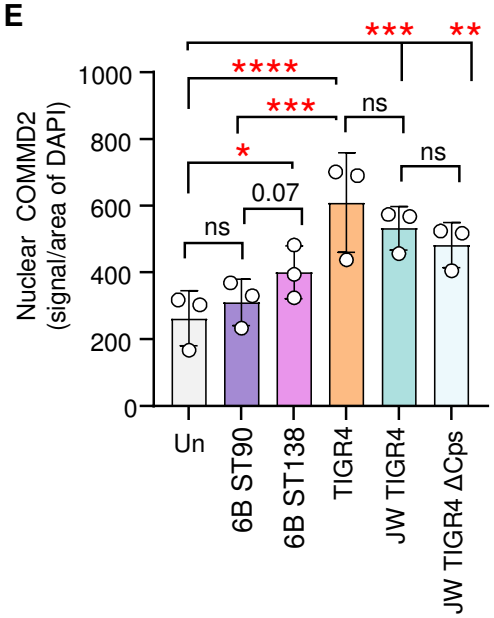

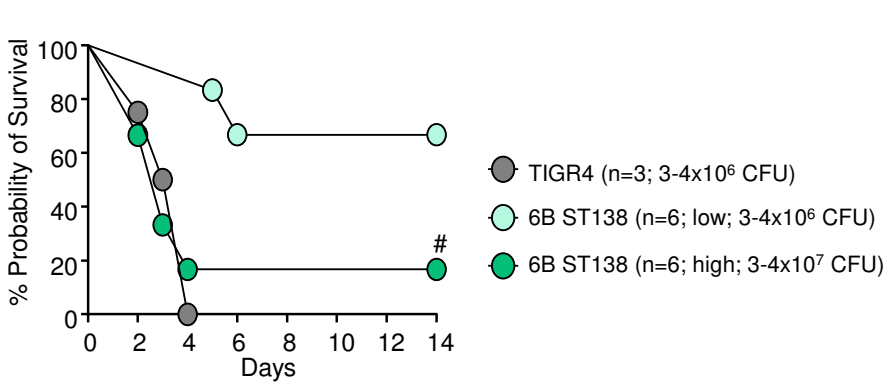

Holm-Šídák's multiple comparisons test	Summary	Adj. P Value
TIGR4 vs. 6B ST138 (high)	ns	0.8741
TIGR4 vs. 6B ST183 (low)	**	0.0099

CMD2 nuclear translocation screen with pneumococcal mutants and hydrogen peroxide. Sup. FIG 10

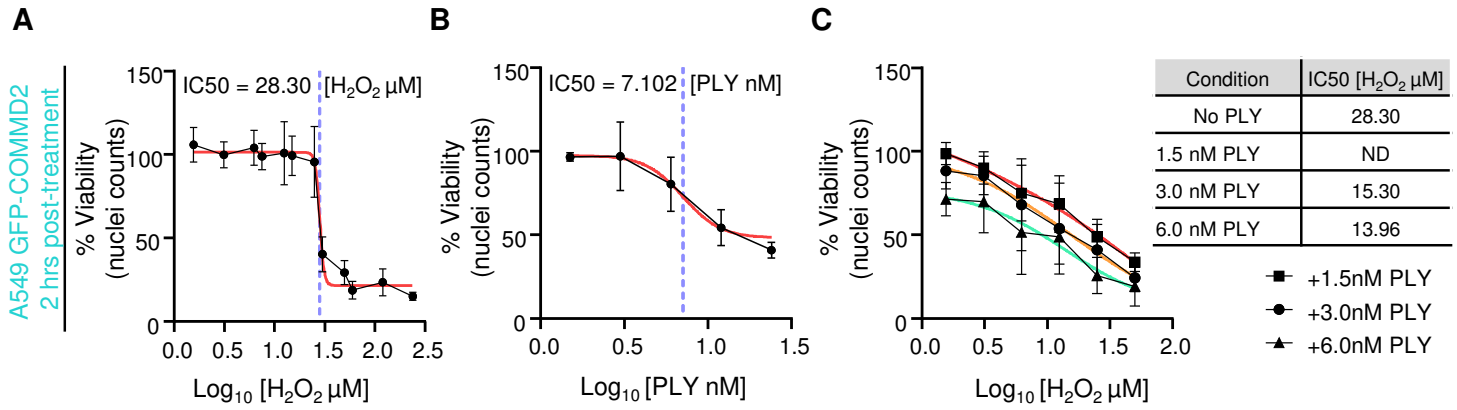
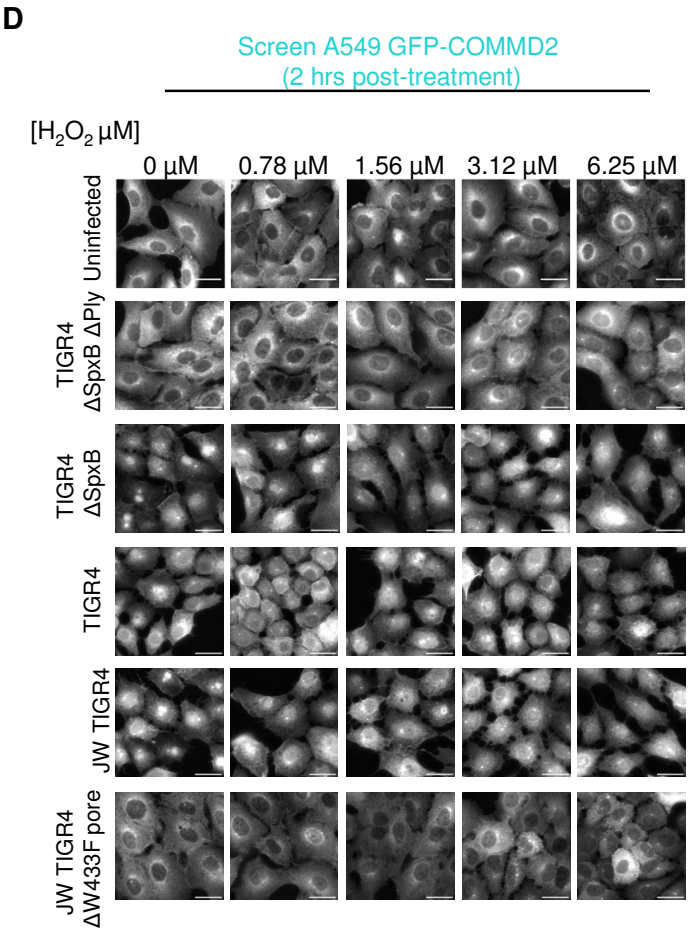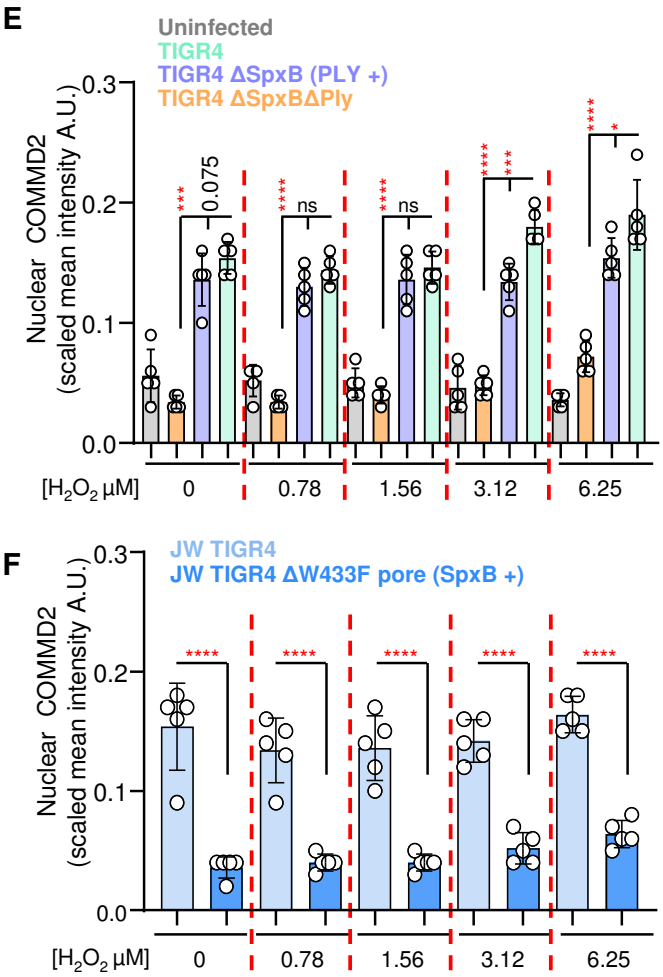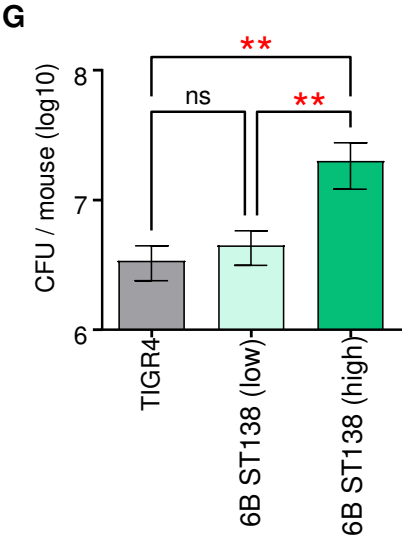
Condition	IC50 [H_2O_2 µM]
No PLY	28.30
1.5 nM PLY	ND
3.0 nM PLY	15.30
6.0 nM PLY	13.96